Available online at www.sciencedirect.com
SCIENCE DIRECT
Polymer 47 (2006) 1226–1244
polymer
www.elsevier.com/locate/polymer

Physical properties of poly(*n*-alkyl acrylate) copolymers. Part 1. Crystalline/crystalline combinations

K.A. O'Leary, D.R. Paul *

Department of Chemical Engineering and Texas Materials Institute, University of Texas at Austin, Austin, TX 78712, USA

Received 28 October 2005; received in revised form 1 December 2005; accepted 2 December 2005
Available online 27 December 2005

Abstract

The physical properties of *n*-alkyl acrylate copolymers containing two crystallizeable monomers, including thermal characteristics, structure as determined by small angle X-ray scattering, and gas permeability as a function of temperature, were examined in detail and compared to the corresponding homopolymers. The copolymers exhibit co-crystallization and, thus, for a given average side-chain length have comparable melting temperatures as the corresponding homopolymers. For a given side-chain length, the copolymers have somewhat lower heats of fusion than the corresponding homopolymers because of a reduction in crystallite size as revealed by SAXS. This depression in crystallinity is reflected in the permeability data for the copolymers. Poly(*n*-alkyl acrylates) exhibit a 'jump' in their gas permeability at the T_m of the side-chain lengths that is mainly caused by a switch in the side-chain morphology from crystalline to amorphous upon melting. The depression in crystallinity for the copolymers results in a smaller permeation jump. The jump breadth correlates with the melting endotherms for these polymers as determined by DSC. Ultimately, the melting endotherms for these copolymer systems provide an excellent tool for predicting permeability changes across the melting region.

Keywords: Poly(*n*-alkyl acrylates); Gas permeation; Physical properties

1. Introduction

The physical properties of poly(*n*-alkyl acrylates) have been of continuing interest since they were first investigated in the 1940s by Rehberg and Fisher [1]. Unlike conventional crystalline polymers where the backbone crystallizes, it is the long *n*-alkyl side-chains of these polymers that crystallize [2–8]. The melting-crystallization of the long side-chains, which occurs at a melting temperature (T_m) that can be controlled by side-chain length, causes significant changes in the physical properties of the polymer. Much of the research on *n*-alkyl acrylate homopolymers to date has focused on the glass transition and melting temperatures, heats of fusion, crystalline structure, mechanical properties, adhesion, and more recently gas transport properties [1,3–15]. Mogri and Paul have shown the gas permeability of poly(*n*-alkyl acrylates) is typical of classical polymers above and below the T_m. Poly(*n*-alkyl acrylates), however, exhibit a distinct 'jump' in permeability at the T_m as large as three orders of magnitude [4,5,8,16]. The unusual temperature-dependant physical properties of these polymers make them ideal for many industrial applications including uses as platforms for catalysts, agricultural seed coatings, medical delivery applications, and membranes for modified atmospheric packaging (MAP) of produce [7,10,17–19].

Fruits and vegetables are typically packaged in passive containers; however, there is growing interest in more active packaging concepts. The respiration rate of post-harvest produce is dependant on many conditions, including temperature, gas exposure, ripeness, and type of produce [19,20]. MAP is a packaging method which utilizes a gas exchange membrane to maintain the concentrations of gases, typically oxygen and carbon dioxide, in the packaging surrounding the produce within an optimal range for prolonged freshness [17,20–24]. The respiration rate of produce is significantly more dependent on temperature than is the permeability of traditional polymers; this renders them inadequate as membrane materials when shipping, storing, or marketing involves widely varying temperature ranges because the changes in consumption of O_2 and the production of CO_2 by the produce cannot be matched by permeation through the membrane. The permeability 'jump' of these long side-chain acrylates offers interesting possibilities for use as a membrane materials in such cases [7,10,11,17]. While the homopolymers of *n*-alkyl acrylates have a very distinct and immediate jump at their melting points, combinations of these

* Corresponding author. Tel.: +1 512 471 5392; fax: +1 512 471 0542.
E-mail address: drp@che.utexas.edu (D.R. Paul).

0032-3861/$ - see front matter © 2005 Elsevier Ltd. All rights reserved.
doi:10.1016/j.polymer.2005.12.005

polymers in the form of copolymers, blends, and/or laminates may allow avenues for engineering membrane materials that have a temperature-permeability dependence similar to that of the respiration rate of specific produce types. This paper is the first in a two part series examining the permeability properties of *n*-alkyl acrylate copolymers. This paper primarily deals with cases where both homopolymers crystallize; the next paper will consider copolymers systems where only one of the homopolymers is crystallizeable.

2. Experimental

2.1. Polymer synthesis and characterization

All of the polymers used in this work were prepared in a three-step process including monomer purification, polymer synthesis, and polymer purification which has been described in detail in prior papers [4,5,8]. Dodecyl (A12), tetradecyl (A14), octadecyl (A18), and behenyl (A22) acrylate monomers were generously donated by Landec Corporation while decyl (A10) acrylate was purchased from Scientific Polymer Products. All monomers were initially purified over alumina oxide. Solution polymerizations were performed in toluene at 60 °C for 24 h to obtain 100% conversion. The monomer mixtures were prepared at 25 mol% increments ranging from 0 to 100% while initiator and solvent concentrations were fixed at approximately 0.2 and 65 wt% of monomer, respectively. The polymers were precipitated into ethanol and then further purified by dissolving in toluene with re-precipitation into ethanol three times. The polymers were finally placed in a 60 °C vacuum oven to strip any remaining solvent.

A prior study demonstrated that the reactivity ratios of the various combinations of acrylate monomers were unity within experimental error which eliminates the possibility of composition drift during the free radical copolymerization [8]. Thus, the copolymer compositions can be taken to be equal to the monomer concentrations used in the polymerizations. All compositions were determined via ^{13}C NMR using a method described previously [8].

2.2. Gel permeation chromatography

Gel permeation chromatography (GPC) was conducted using an Agilent 1100 chromatograph with 20 μl of polymer solution made from approximately 10 mg of polymer per 2 ml GPC grade THF. They were filtered with a Whatman 0.2 μm PTFE membrane syringe filter and run at room temperature. The samples were analyzed using a calibration with polystyrene standards.

2.3. Sample construction for gas permeation measurement

Permeability measurements were made on films formed from various compositions of P(A14-*co*-A18), P(A12-*co*-A22), and P(A10-*co*-A18) using techniques described previously [4,5,8,9]. Films of these polymers were supported during the permeation measurements by coated ceramic Anopore® discs (Whatman).

Polymer films were cast by two different methods depending on their morphology at room temperature. Polymers that were solid at room temperature, PA 18, PA 22, P(A14-*co*-A18) 25/75 and 50/50, P(A12-*co*-A22) 25/75 and 50/50, and P(A10-*co*-A18) 25/75%, were solution cast from toluene using a casting ring sitting on a silicon wafer. These films were floated off the wafer into a chilled water bath. Polymers that were molten at room temperature, PA 10, PA 12, PA 14, P(A12-*co*-A22) 75/25, and P(A10-*co*-A18) 75/25 and 50/50%, were melt cast in a 60 °C oven directly onto the coated ceramic support. The 75/25% sample of P(A14-*co*-A18) had a melting temperature at room temperature, which caused the morphology to change with slight temperature changes in the lab. This polymer was solution cast using the same technique employed for other solid polymers except that after the solvent evaporated, the sample was placed into a laboratory freezer to insure it was crystalline before it was placed in the ice bath for removal from the silicon wafer.

Solid film thicknesses were measured using an Ames Micrometer prior to permeation experimentation while the molten film thickness was determined by performing a simple mass balance calculation involving the measured mass of polymer, the estimated density of the amorphous polymer (0.986 g/cm^3), and the known diameter of the ceramic support (47 mm).

The permeation sample construction developed by Mogri and Paul was utilized to establish a known sample area and uniform film thickness over a range of temperatures necessary for accurate permeability measurements [4,5,9,16]. A porous ceramic Anopore® disc was used to provide mechanical support for the polymer film. The ceramic disc was razor coated with a trichloroethylene solution of poly(2,6-dimethyl-1,4-phenylene oxide) (PPO), generously donated by GE Plastics (M_w = 46,000, intrinsic viscosity = 0.46 dl/g); this coating was used to impede the molten polymer from flowing into the pores during permeation experiments at temperatures above the melting temperature of the sample. A permeance resistance model was used to subtract out the effects of the PPO layer. All polymers were melted and then cooled at 1 °C/min to ensure a controlled thermal history for crystallization. Permeation tests were made by progressively raising the measurement temperature to higher levels. Detailed casting techniques are described in the literature [4,5,8,9,16]. The gases used, He, H_2, O_2, N_2, CH_4, and CO_2, were purchased from Matheson Tri Gas with at least 99.9% purity and were run at a 2 atm upstream pressure for all temperatures.

2.4. Differential scanning calorimetry

Differential scattering calorimetry (DSC) was conducted using a Perkin–Elmer DSC 7 with polymer samples weighing approximately 15 mg. All samples were initially heated to well above their melting temperatures at 20 °C/min, cooled below their T_m at 1 °C/min, and reheated at 10 °C/min. All thermal characteristics reported in this work were taken during the second heating.

2.5. SAXS characterization

Small angle X-ray scattering (SAXS) was performed using a MolMelt SAXS equipped with a liquid sample holder. Samples consisted of about 50 mg of polymer and as many as four samples could be loaded into the sample holder at a given time. The temperature was controlled with a Fisher Brand refrigerated circulator that circulated fluid through the sample holder, around the samples. Although only the sample holder temperature could be measured, all temperature adjustments were held for 12 h before any experiments were run to ensure thermal equilibrium between the sample holders and the polymer samples. Upon loading the samples, the temperature of the sample holder was heated to some temperature 10 °C above the T_m of the polymer with the highest melting temperature. This temperature was held for 6 h and then cooled to the appropriate experimental temperature ensuring a uniform thermal history for all samples characterized. All data were collected over a real time of 2 h and analyzed using the FIT2D software program written by Hammersley available on the FIT2D-ESRF website.

3. Thermal behavior

3.1. Homopolymers

The melt temperatures and heats of fusion of various poly(*n*-alkyl acrylate) were characterized using DSC and are shown in Fig. 1(a) and (b), respectively, as a function of the number of carbon atoms in the side chain, *n*; also see Table 1. All data were measured on the second heating. The heat of fusion, ΔH_f, is shown in units of kJ/mol of monomer repeat units because these units give a useful linear relationship with side-chain length; whereas, the heat of fusion per unit mass of polymer is clearly non-linear in *n*. The results from this study agree well with previous reports in the literature [3,5–7,11,15,18]. Slight deviations among the various data sets may be attributed to experimental methods of analysis including thermal history or baseline approximation.

Regression lines were drawn through the T_m and ΔH_f data in Fig. 1 for subsequent use in comparing copolymers. The melt temperatures of the homopolymers increase with side-chain length following a second order polynomial trend. The heats of fusion increased linearly with side-chain length when plotted in units of kJ/mol.

$$\Delta H_f = 3.54n - 33.4 \quad (1)$$

The linear equation goes to $\Delta H_f = 0$ at a value of *n* equal to 9.4. The minimum side-chain length needed for crystallization reported in the literature ranges from 8 to 9.2 [3,6]. According to Eq. (1), PA 10 should be a crystallizeable polymer, while all polymers with fewer carbons in their side chains should not. Due to equipment limitations, we are not able to make measurements on PA 10 in the crystalline state. Since this value of n is near the border of crystallizeable/non-crystallizeable polymers, copolymers containing the alkyl acrylate with $n = 10$ have been included in both categories. This paper deals with copolymers where all the acrylate monomers have side-chain lengths of 10 and greater, while the second paper in this series will deal with copolymers where one of the acrylate monomers has side-chain lengths of 10 and less.

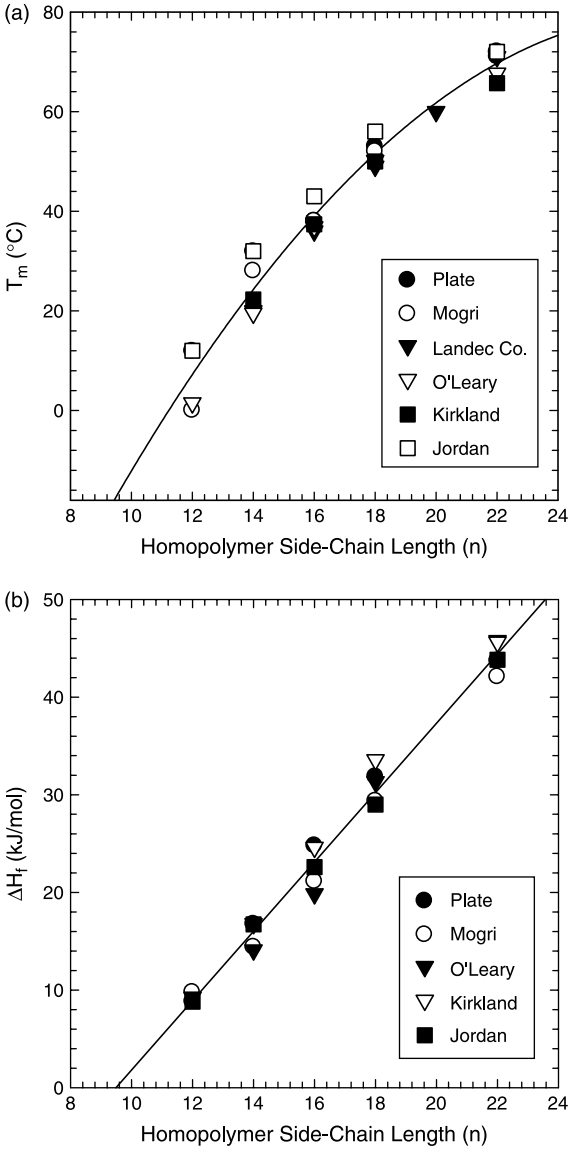

Fig. 1. T_m (a) and ΔH_f (b) of *n*-alkyl acrylate homopolymers versus side-chain length (*n*). Data from this work as well as from the literature are shown [3,5–7,11,15,18].

3.2. Copolymers

Thermal analyses of copolymers were performed in the same manner as for homopolymers. Table 2 lists the melt temperature, heat of fusion, and molecular weight of the copolymers examined in this study. An average side-chain length $\langle n \rangle$ was defined as follows

$$\langle n \rangle = x_1 n_1 + x_2 n_2 \quad (2)$$

Table 1
Melting temperature, heat of fusion, and molecular weight data for poly(*n*-alkyl acrylate) homopolymers

Homopolymer	Side-chain length (*n*)	T_m (°C)	ΔH_f (kJ/mol)	Polymer $\bar{M}_w$	Repeat unit molecular weight (g/mol)
PA 10	10	–	–	112,000	212
PA 12	12	1.5	9.3	165,000	240
PA 14	14	19.5	14.1	245,000	268
PA 16	16	36.4	23.1	161,000	296
PA 18	18	50.2	31.3	106,000	325
PA 22	22	67.7	45.8	[a]	381

[a] $\bar{M}_w$ could not be measured since PA 22 is no soluble in THF.

where x_1 is the mole fraction of monomer one having n_1 side-chain carbons and $x_2 = (1 - x_1)$ is the mole fraction of monomer 2 having n_2 side-chain carbons; this quantity is useful for analyzing the data.

In principle, crystallization of copolymers, whether the crystallizing units are in the main chains or side chains, can form two extremes of behavior. The most common is where the presence of the minor component causes melting point depression of the major component as described by simple theories [25–28]. Typically when both units are capable of crystallizing, the melting point shows depressions on both sides of the T_m composition diagram resembling a eutectic while crystallinity may go to zero, or reach a minimum, in the mid-composition range. The other is where the two units co-crystallize with the typical signature of a steady, monotonic progression of the melting point and heat of fusion from that of the one homopolymer to that of the other as composition changes [27–34]. As will be shown in the following, this is the more common situation in the copolymers described here. However, there are clearly intermediate situations that are somewhat more difficult to categorize. The following gives a rather detailed analysis of the thermal properties of the current copolymers as this is useful for interpreting their gas permeation characteristics.

Sample DSC endotherms for two copolymers systems are shown in Fig. 2(a) and (b). The endotherms qualitatively reflect the distribution of crystallite sizes. In general, as the side-chain lengths for *n*-alkyl acrylate homopolymers increase, the more methylene units in each repeat unit are able to crystallize causing larger crystallites to form having a more uniform size distribution and a higher melting point. As the side chains become shorter, the number of carbons entering the lattice decreases causing a broader distribution of smaller crystallites and a correspondingly lower melting point. Fig. 2(a) shows endotherms for copolymers of P(A14-*co*-A18) polymerized in molar increments of 25% ranging from 0 to 100. There is a steady progression of peak location, width, and height for the copolymers ranging from PA 14 to PA 18 consistent with the

Table 2
Melting temperature, heat of fusion, and molecular weight data for poly(*n*-alkyl acrylate) copolymers

Copolymer	Mol% monomer 1[a]	Average side-chain length $\langle n \rangle$	T_m (°C)	ΔH_f (kJ/mol)	Copolymer M_w
P(A10-*co*-A14)	75	11	–	–	215,000
	50	12	3.7	4.8	141,000
	25	13	11.9	9.5	191,000
P(A10-*co*-A18)	75	12	−1.1	7.6	185,000
	50	14	21.2	11.8	235,000
	25	16	38.5	21.3	197,000
P(A14-*co*-A18)	75	15	25.7	17.4	468,000
	50	16	32.7	20.8	119,000
	25	17	41.7	24.5	109,000
P(A10-*co*-A22)	75	13	6.4	10.3	192,000
	50	16	35.5	13.3	118,000
	25	19	50.5	21.0	138,000
P(A12-*co*-A22)	75	14.5	21.0	12.9	338,000
	50	17	44.2	17.0	102,000
	25	19.5	56.0	25.4	108,000
P(A14-*co*-A22)	75	16.5	30.2	16.0	161,000
	50	19	44.0	18.1	115,000
	25	21.5	54.9	27.8	108,000
P(A16-*co*-A22)	75	17.5	40.7	21.5	121,000
	50	19	48.2	24.6	116,000
	25	20.5	57.2	30.2	100,000
P(A18-*co*-A22)	75	19	53.4	28.2	100,000
	50	20	56.9	31.9	111,000
	25	21	61.5	35.6	173,000

[a] Note that monomer 1 refers to the first monomer listed in the copolymer, i.e. for P(A14-*co*-A18), monomer 1 refers to A14.

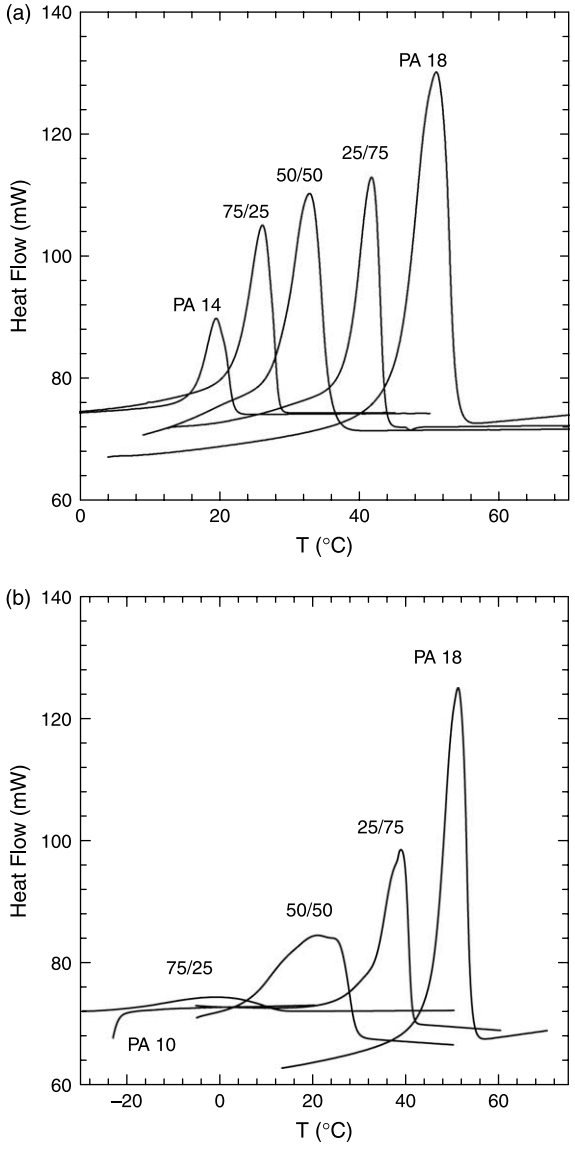

Fig. 2. DSC endotherms for various compositions of P(A14-*co*-A18) (a) and P(A10-*co*-A18) (b) copolymers.

progression of a corresponding series of *n*-alkyl acrylate homopolymers. This indicates that the two types of units co-crystallize as expected from the literature [5]. Fig. 2(b) shows endotherms for copolymers of P(A10-*co*-A18) in molar increments of 25% ranging from 0 to 100. As explained earlier PA 10 does not crystallize in the temperature range examined here. In principle, A10 units have perhaps only one carbon in its side chain for co-crystallizing with A18 units. There is also a distinct possibility that the A10 units do not co-crystallize with the A18 units at all, but rather act as a non-crystallizeable spacer that more appropriately might be thought of as a melting point depression phenomenon. This possibility will be addressed more thoroughly in part 2 of this series. In any case, as the concentration of A10 in the copolymer increases, the crystallites become smaller and have a broader distribution of size or perfection as reflected by the lowering and broadening of the endotherms with increasing A10 concentration.

Figs. 3 and 4 summarize the melting behavior of a number of copolymers of *n*-alkyl acrylates, where the *n* for each is always 10 or higher, by plotting T_m and ΔH_f versus the copolymer composition. For all cases when *n* is larger than 10 for each *n*-alkyl acrylate monomer, we see a characteristic signature of co-crystallization in that both T_m and ΔH_f are monotonic functions of composition. The copolymer melting point may lie slightly above or below the line connecting the homopolymer values when plotted versus mole fraction depending on the values of n_1 and n_2. On the other hand, ΔH_f always lies below the line suggesting that copolymerization generally leads to less crystallinity than expected; however, the extent of this departure depends on n_1 and n_2.

For copolymers containing A10, the T_m and ΔH_f versus composition relations are also monotonic but tend to show

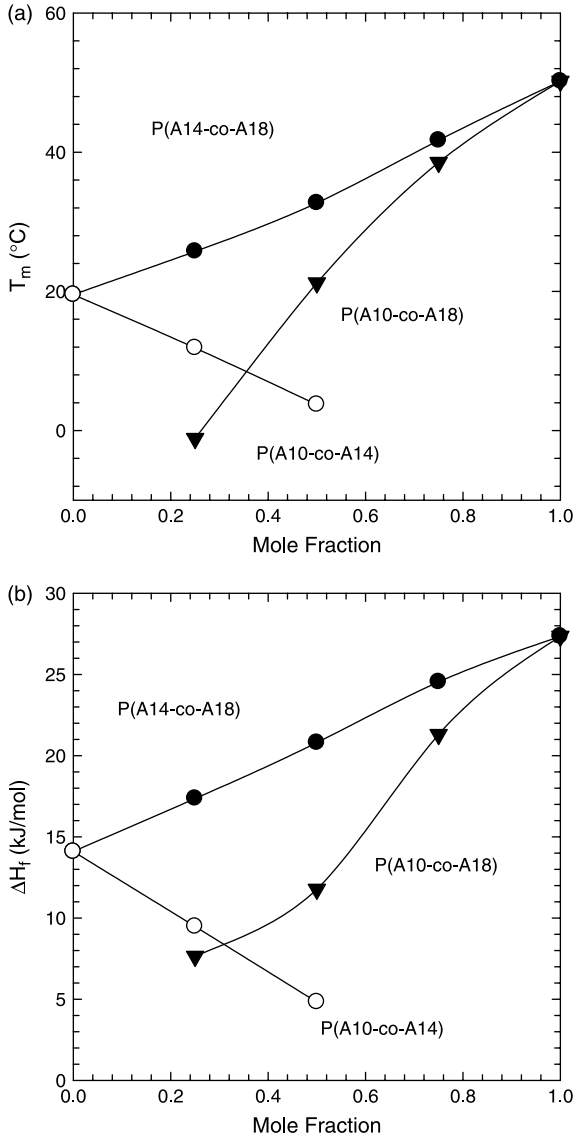

Fig. 3. Dependence of T_m (a) and ΔH_f (b) on copolymer composition for materials based on monomers A10, A14, and A18.

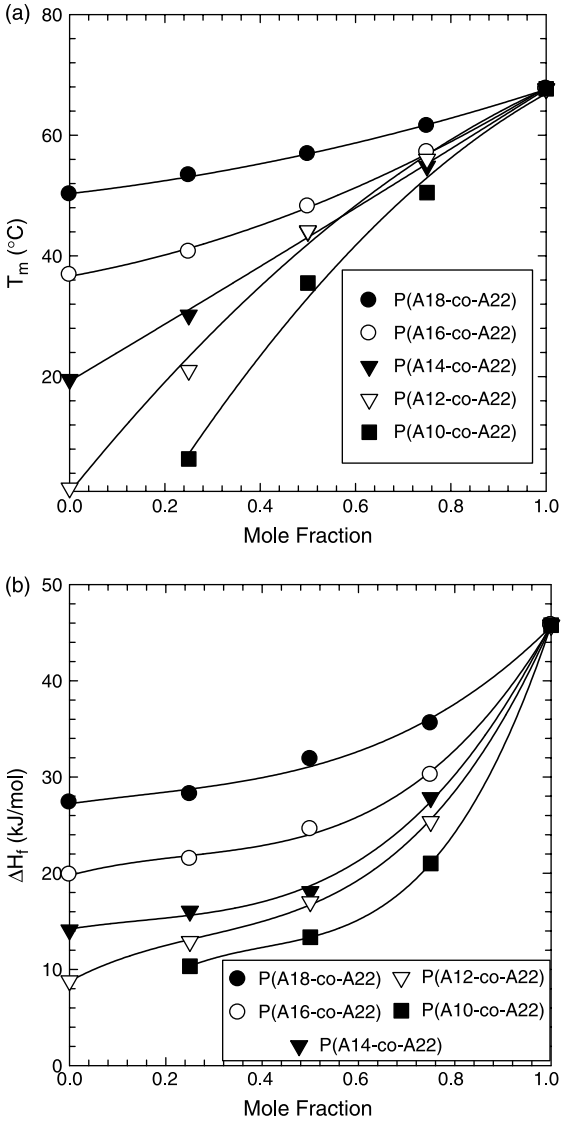

Fig. 4. Dependence of T_m (a) and ΔH_f (b) on copolymer composition for materials based on monomer A22 and other *n*-alkyl acrylate monomers.

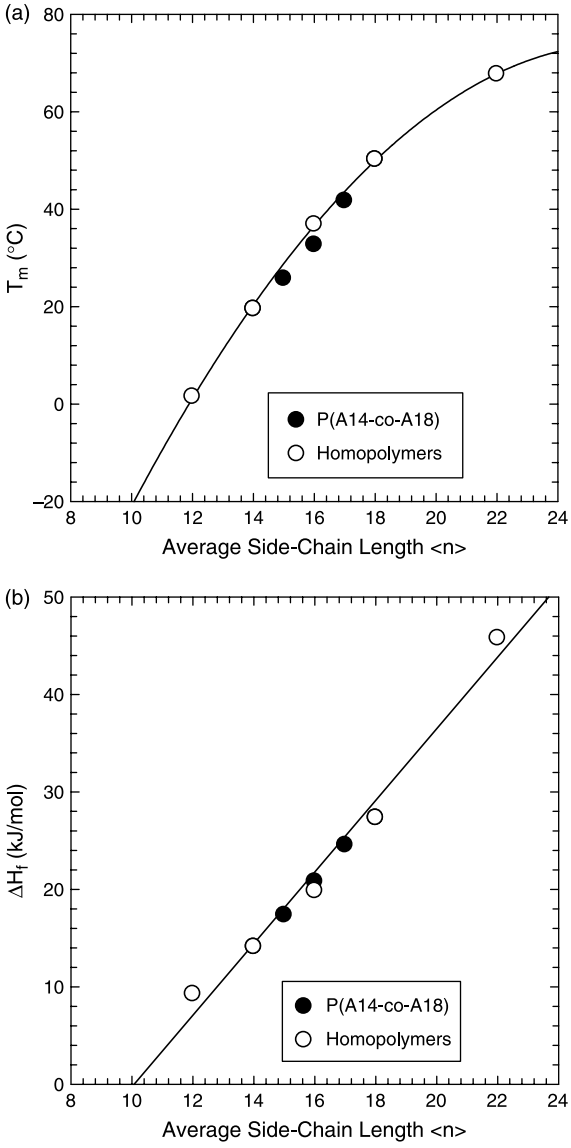

Fig. 5. Homopolymer and P(A14-*co*-A18) copolymer comparisons for melting temperature (a) and heat of fusion (b) shown as a function of the average side-chain length of the copolymer or side-chain length of the homopolymer.

slightly different patterns particularly as the other monomer unit has shorter side chains. For example, if we extrapolate the homopolymer T_m data in Fig. 1(a) to $n=10$ we get $T_m \approx -12$ °C. The T_m data for A10 copolymers with A18 and A22 appear to be going to a much lower intercept, in the 100% A10 limit, than this. Copolymers of A10 and A14 show $\Delta H_f = 0$ even when there is 25 mol% A14 in the material, see Fig. 3(b). On the other hand, copolymers of A10 with A18 and A22 seem to be headed to a finite ΔH_f in the limit of 100% A10.

The copolymer thermal properties relationships are more critically analyzed with respect to the behavior of homopolymers of similar side-chain lengths in Figs. 5–7, using plots versus n for the homopolymer and $\langle n \rangle$ for the copolymers. Fig. 5 compares T_m and ΔH_f results for P(A14-*co*-A18) copolymers with those of homopolymers. The open circles represent the homopolymer data while the closed circles correspond to the results for the copolymers. For this system, both T_m and ΔH_f track closely along the trend established by the homopolymers. The side chains of the two monomers are of similar lengths, both crystallize, and their endotherms from Fig. 2(a) progress in similar shape and size as those of the homopolymers. It is understandable that copolymers of these two similar monomers would thermally behave like a homopolymer with an equivalent side-chain length. Similar plots are shown in Figs. 6 and 7 for P(A12-*co*-A22) and P(A10-*co*-A18) copolymers. In both systems, the copolymer T_m results are also in close agreement with the homopolymer T_m results; however, the copolymer ΔH_f results are significantly lower than the line established for the homopolymers. Both monomer units in the P(A12-*co*-A22) system are readily crystallizeable while for the P(A10-*co*-A18) copolymers the A10 units are on the border of being crystallizeable. Both

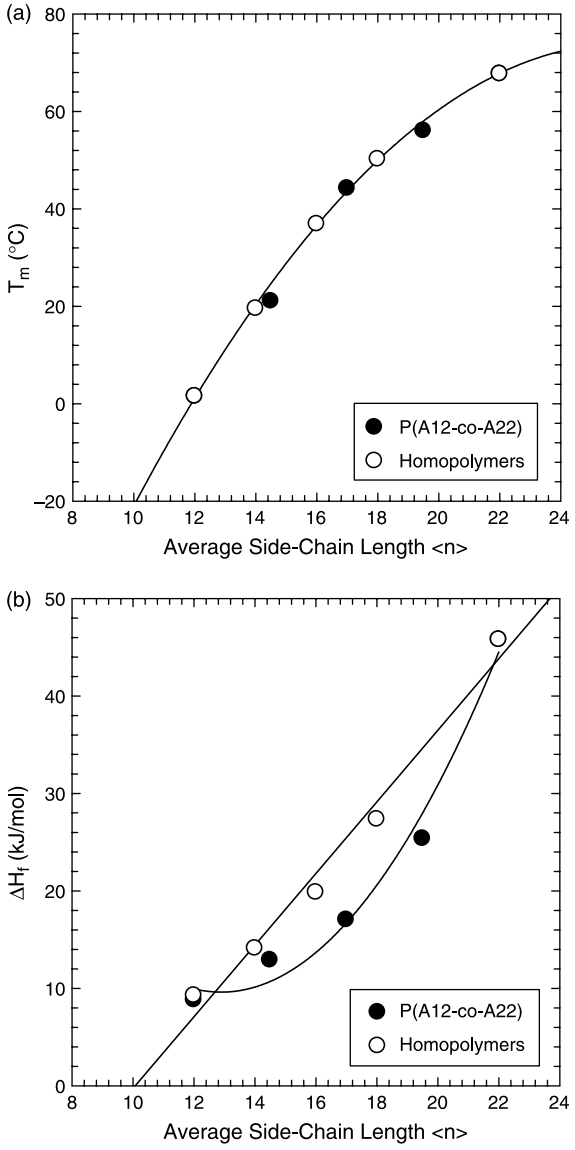

Fig. 6. Homopolymer and P(A12-*co*-A22) copolymer comparisons for melting temperature (a) and heat of fusion (b) shown as a function of the average side-chain length of the copolymer or side-chain length of the homopolymer.

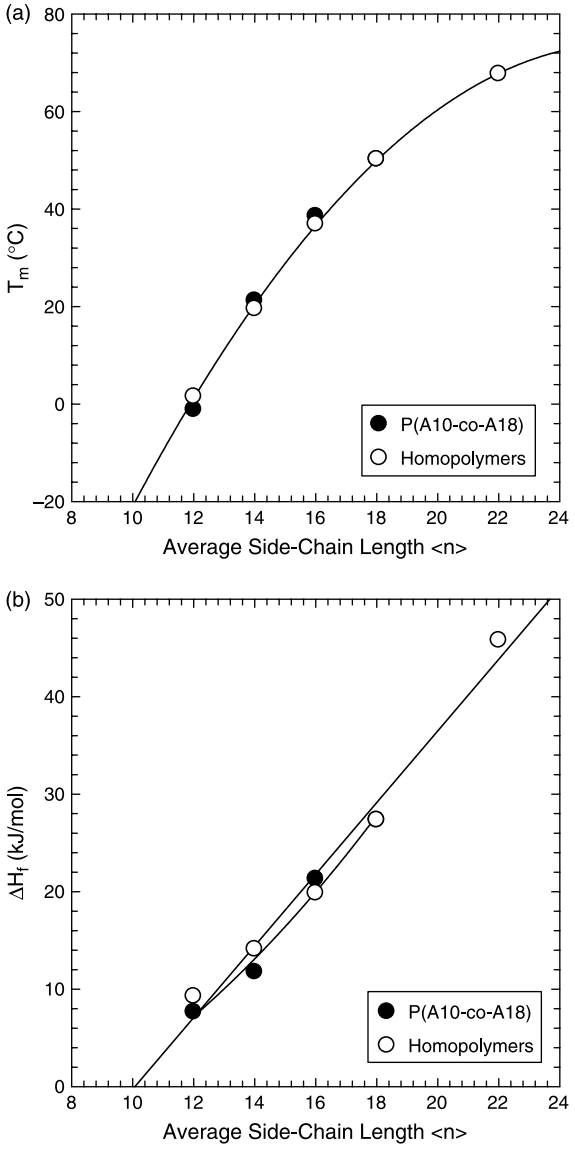

Fig. 7. Homopolymer and (A10-*co*-A18) copolymer comparisons for melting temperature (a) and heat of fusion (b) shown as a function of the average side-chain length of the copolymer or the side-chain length of the homopolymer.

systems have monomers of significantly different side-chain lengths. Their endotherms also resemble those shown in Fig. 2(b) with smaller, broader melting peaks than homopolymers or the P(A14-*co*-A18) copolymer system. These copolymers are able to co-crystallize because of the conformational freedom in the amorphous backbone allowing side-chains of different lengths to crystallize in the same lattice. In the case of P(A12-*co*-A22), both monomers contain reasonably long side-chains in addition to having a side-chain length difference of 10 carbons. This difference may impede and restrict the conformational freedom of the backbone inhibiting the overall crystallinity of the copolymer system as seen by the depressed heat of fusion relative to homopolymers. On the other hand, the P(A10-*co*-A18) system does not show the extent of the ΔH_f depression as the P(A12-*co*-A22) system despite the fact that the A10 units do not readily crystallize on their own.

4. Structural analysis

4.1. Homopolymers

Small angle X-ray scattering (SAXS) was performed on the homopolymers and copolymers in both the amorphous ($T > T_m$) and crystalline ($T < T_m$) states. Fig. 8 shows typical plots of scattering intensity versus the scattering angle, 2θ, for both states. Wide angle X-ray diffraction has revealed that poly(*n*-alkyl acrylates) are paraffin-like in their ability to form hexagonal crystal lattice structures. SAXS provides insight about how the thicknesses of these crystals change with *n*; unfortunately, this technique provides no information about the lateral dimensions of the crystal, which would be needed to determine the aspect ratio that affects permeation in the solid

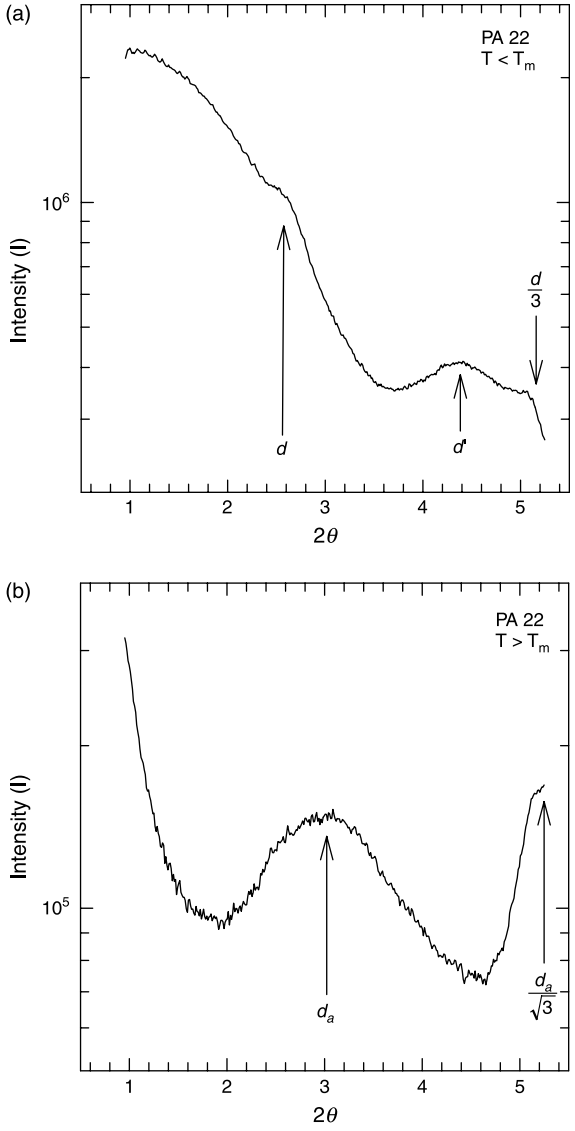

Fig. 8. Typical SAXS intensity versus 2θ plots for poly(*n*-alkyl acrylate) homopolymers. Data shown for crystalline PA 22 ($T<T_m$) (a) and molten PA 22 ($T>T_m$) (b).

form. Hsieh and Morawetz reported a SAXS study using crystalline fibers of PA 16 and PA 18. They found three scattering peaks; two diffuse peaks at 16 and 47 Å as wells as a weak, well-defined, sharp peak at 28 Å for PA 18 [35,36]. The crystalline side-chains pack similar to a lamellar system where the multiple scattering peak spacings progress in the following ratios 1:1/2:1/3:1/4:… [37–39]. In some systems, some of the peaks may be missing owing to a minimum in the form factor scattering [37]. It is proposed that the similarly shaped 16 and 47 Å peaks characterize the same lamellar-like packing form where the 16 Å peak appears to be a third order reflection of the 47 Å peak; the second order peak appears to be missing. The peak at 28 Å is much weaker and shaped differently and does not appear to be a multiple of the other two peaks, therefore, it is interpreted as independent of the other peaks. These two types of reflections suggest two different packing structures: an end-to-end packing of the side chains (Fig. 9(a)) which gives

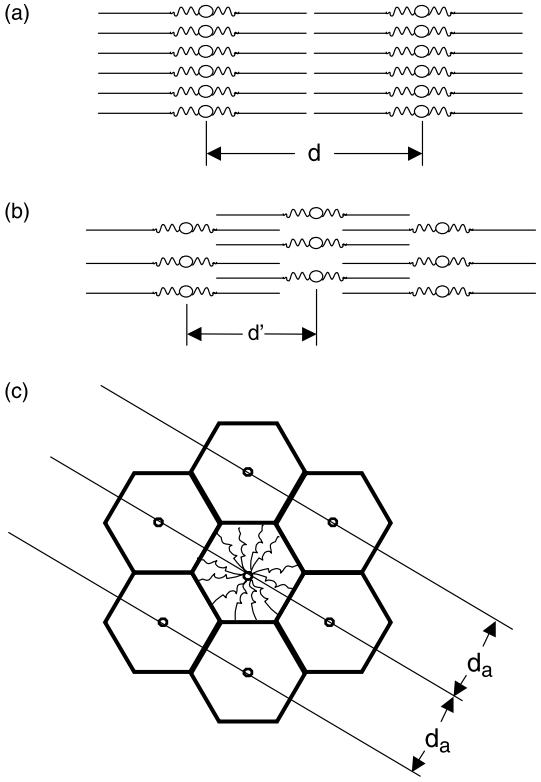

Fig. 9. Schematics of end-to-end (a) and interdigitating (b) side-chain packing proposed by Hsieh and Morawetz for crystalline poly(*n*-alkyl acrylates) where the open circles represent the axes of the polymer main chains with side chains extending out in an all trans conformation in the crystalline region (solid lines); amorphous portion is represented by wavy lines [36]. Proposed hexagonal packing lattice (c) for amorphous *n*-alkyl acrylate polymers where the open circles represent the polymer main chain axes and curvy lines represent the side chains.

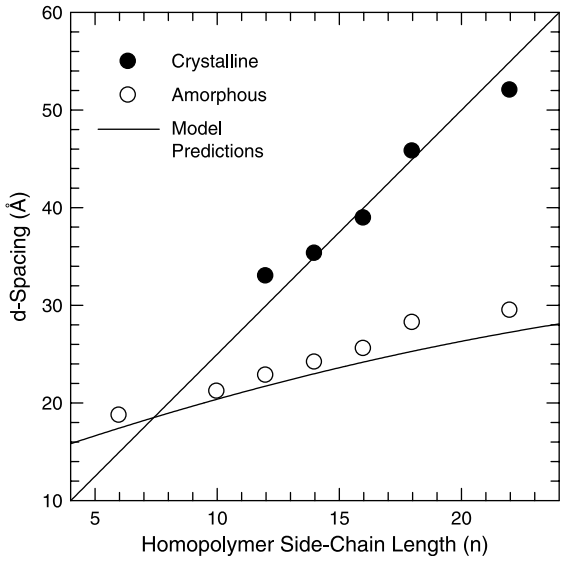

Fig. 10. *d*-Spacing (Å) values for crystalline and amorphous *n*-alkyl acrylate homopolymers as a function of side-chain length measured by SAXS (points) and calculated from model predictions (lines). According to the interpretation given in the text, the crystalline values correspond to *d* as defined in Figs. 8(a) and 9(a) while the amorphous values correspond to *d* as defined in Figs. 8(b) and 9(b).

rise to the 16 and 47 Å peaks and an inter-digitating structure (Fig. 9(b)) that leads to the 28 Å peak [35,36]. Later work by Plate showed that poly(*n*-alkyl acrylates) exhibit an increase in *d*-spacings for both packing structures as the side chains become longer [3]. Fig. 8(a) shows the SAXS intensity versus 2θ for crystalline PA 22 examined over a *d*-spacing region of 16–100 Å. The crystalline sample of PA 22 illustrates the two types of packing reported in the literature. In this figure, the peaks labeled *d* and *d*/3 correspond to the 47 and 16 Å peaks Hsieh observed for PA 18 while d' corresponds to the equivalent peak for PA 22 as the 28 Å peak for PA 18. It should also be noted that the 16 Å peak observed for PA 18 is at approximately 17.5 Å for PA 22 and can, therefore, be seen in Fig. 8(a); this was the only polymer whose *d*/3 peak was within the experimental range analyzed here. The relationship between the spacings for the *d* peak and the homopolymer side-chain length, *n*, is shown in Fig. 10; these results are similar to those reported in the literature [3,35,36]. As the side chains become longer, this *d*-spacing increases, indicating the crystallites become thicker with increasing *n*. The linear relationship between heat of fusion and the crystalline *d*-spacing in Fig. 11(a) clearly illustrates a direct correlation between the two as might be expected.

A simple mathematical model was developed to describe the *d*-spacings for the crystalline polymers with side-chains arranged in an end-to-end packing structure. It was assumed, as shown in Fig. 9(a), that the *d*-spacing of the polymers is the distance between the main chains, shown as open circles in the schematic. Assuming an all trans conformation between the crystallizeable carbons ($n-9.4$), each methylene pair in the crystalline region contributes two times the projected carbon–carbon bond length, i.e. 2(1.25 Å), to the thickness of the crystal. Note that in this packing arrangement, increasing *n* by one adds two methylene units to the crystals. An additional length, β_0, is added to account for the amorphous regions, i.e.

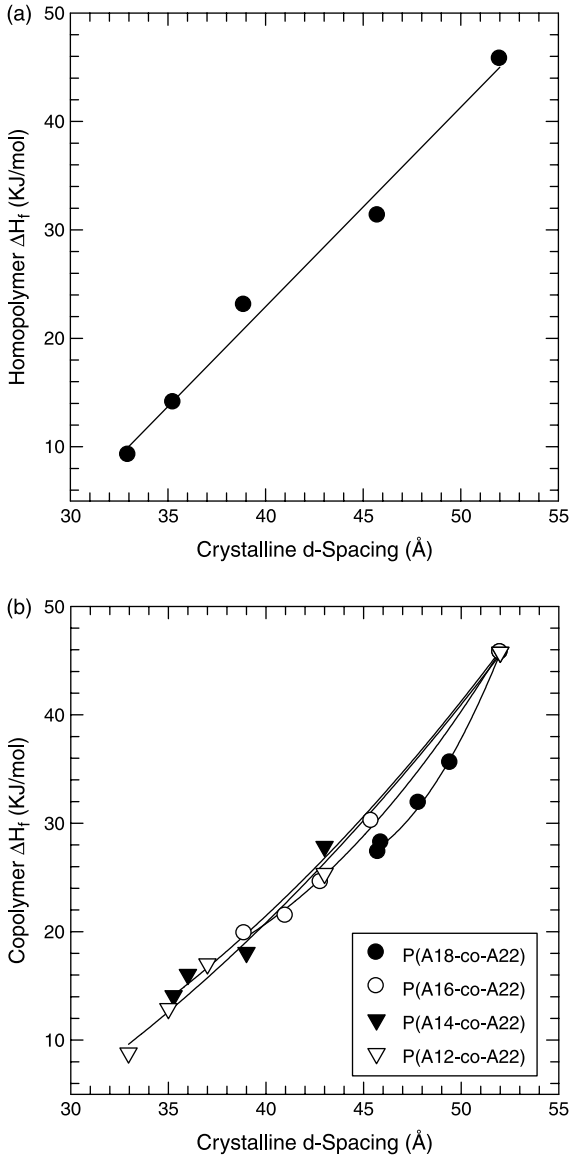

Fig. 11. Relationships between ΔH_f and crystalline *d*-spacing for homopolymers (a) and copolymers (b) of A 22.

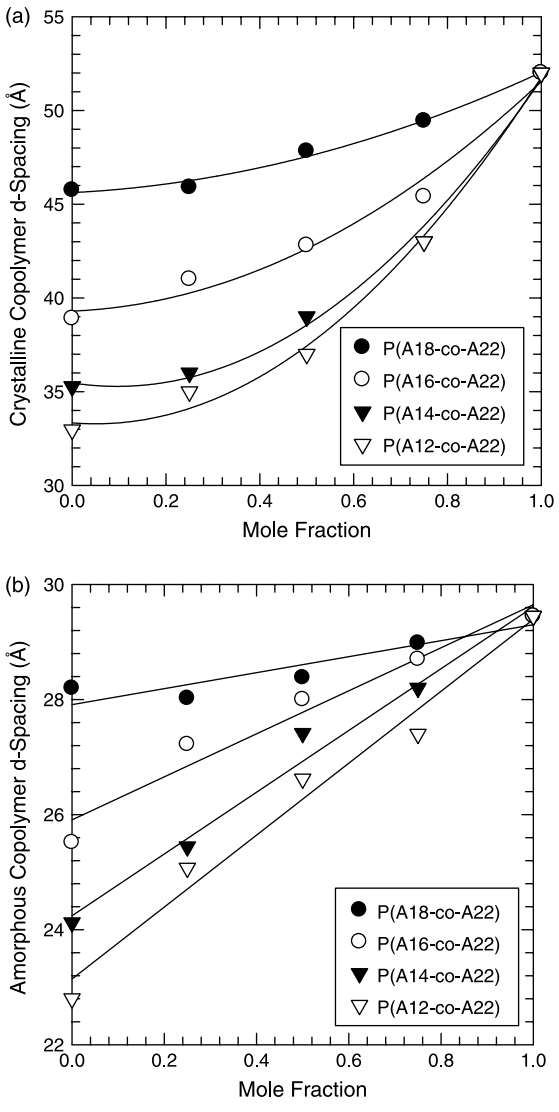

Fig. 12. Relationship between *d*-spacings and copolymer composition in the crystalline (a) and amorphous (b) states for various copolymers based on A22.

$$d = (2)(1.25)(n-9.4) + \beta_0 \quad (3)$$

This latter parameter was estimated using a least squares fit of the experimental SAXS data to Eq. (3) where the slope of d versus n was constrained to be 2.5 Å as explained above. The result is

$$d = 2.5(n-9.4) + 23.5 \quad (4)$$

which provides a reasonably good fit to the experimental results as seen in Fig. 10.

SAXS experiments were also performed on amorphous poly(n-alkyl acrylates) in order to explore any local order in the molten state. An earlier study of amorphous acrylates by Plate reported only a single broad, weak peak in the amorphous state [3]. Fig. 8(b) shows the scattering intensity for amorphous PA 22 plotted as a function of 2θ, where there is a peak at $2\theta \sim 3°$ that shifts to smaller angles for poly(n-alkyl acrylates) with smaller values of n. The open circles in Fig. 10 show the d-spacings computed from the amorphous scattering peaks from the various homopolymers at $T > T_m$. This d-spacing increases with n but with a different slope than the peaks observed at $T < T_m$. Molten PA 22 shows another peak on the edge of the range that can be measured by this instrument. This peak is never visible for lower values of n. We propose the following interpretation of these results and suggest a simple model that seems to confirm the picture.

Fig. 9(a) asserts that the axes of the main chains (circles in Fig. 9) are forced to line up with a close lateral spacing because

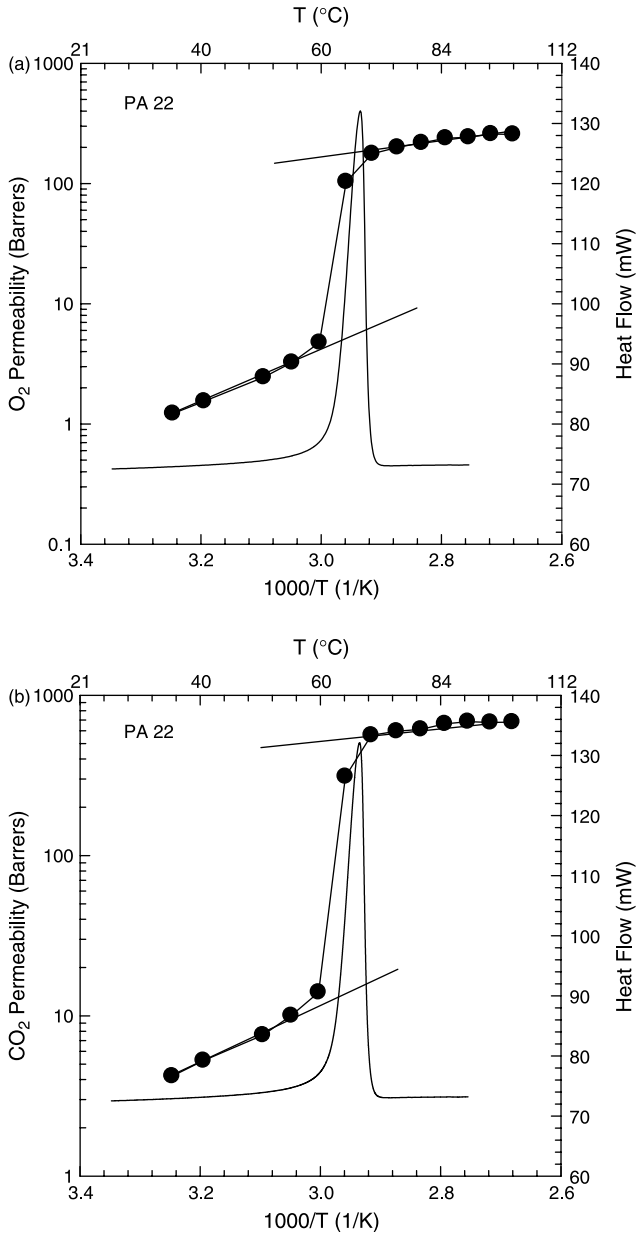

Fig. 13. Gas permeability coefficients as a function of temperature (on Arrhenius coordinates) through the melting temperature region for PA 22 for O_2 (a) and CO_2 (b) with DSC scans superimposed.

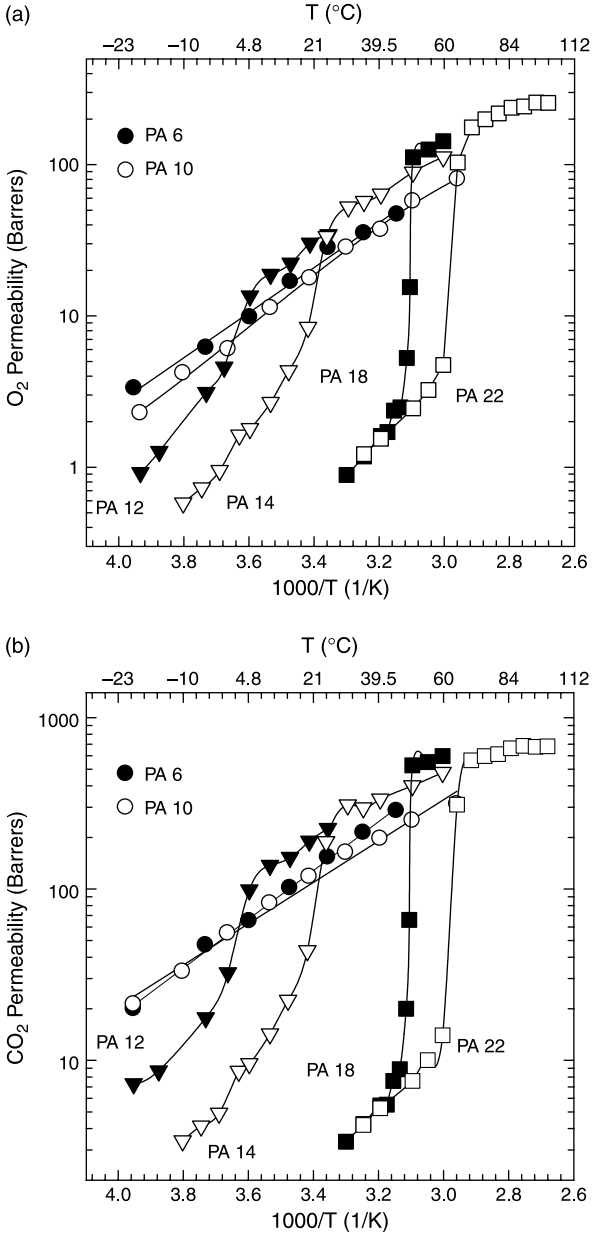

Fig. 14. Permeability of O_2 (a) and CO_2 (b) for homopolymers with side-chain lengths ranging from 6 to 22 carbons as a function of temperature on Arrhenius coordinates.

of the constraints imposed by forming side-chain crystals. However, the latter constraints are removed upon melting; hence, the main chain axes move apart while the side chains take on random conformations radiating away from the backbone in all directions to fill up the space between the main chains. We assume there is some local short order in which the main chain axes are parallel to each other for short distances and arrange in a more or less hexagonal close packing arrangement as suggested in Fig. 9(c). We further assume that the SAXS scattering reflects the *d*-spacings between main chains as schematically illustrated in Fig. 9(c). The scattering should, thus, be similar to that from hexagonally close-packed cylinders where the scattering peak position ratios progress as $1 : (1/\sqrt{3}) : (1/2) : 1/\sqrt{7} : \ldots$ [37–39]. Thus, in Fig. 8(b), we label the two peaks mentioned as d_a and $d_a/\sqrt{3}$. We assume that the peak in the center of the figure represents the first peak. The second peak at the far right of the figure, on the edge of the experimental data, labeled $d_a/\sqrt{3}$, represents the second order of the first peak, d_a. Thus, we focus on the peak labeled d_a for the following analysis. In summary, we assume that both peaks measure the same repeat hexagonal ordering of the main chain axes and their spacings are simply ratios of each other.

The following provides a simple model for estimating the characteristic *d*-spacing defined by the model in Fig. 9(c). The cross-sectional area, *A*, for each main chain is that of the hexagon shown there which, by simple geometry, is related to d_a as follows

$$A = \frac{2}{\sqrt{3}} d_a^2 \tag{5}$$

Consequently, the volume occupied by each *n*-alkyl acrylate repeat unit, *V*, can be obtained by assuming the main chain carbons are in an approximate trans-conformation, i.e. axial length = 2(1.25 Å), such that

$$V = (2)(1.25\ \text{Å})\left(\frac{2}{\sqrt{3}} d_a^2\right) \tag{6}$$

The mass within this volume, in atomic mass units, can be computed by multiplying the molecular weight of each repeat unit by three, which is the number of main chains within each hexagonal unit, i.e.

$$\text{mass} = 3(72 + 14n) \tag{7}$$

The ratio of the mass to the volume of a repeat unit, after appropriate unit conversions, can be set equal to the

Table 3
Activation energy and permeation data extrapolated to 35 °C for various gases through poly(*n*-alkyl acrylate) homopolymers

Homopolymer		Gas					
		He	H_2	O_2	N_2	CH_4	CO_2
PA 6	E_a	6.5	6.7	6.8	8.0	6.8	6.5
	E_c	–	–	–	–	–	–
	P_{35}^+	49.8	89.8	35.3	13.9	31.6	211.7
	P_{35}^-	–	–	–	–	–	–
	P_{35}^+/P_{35}^-	–	–	–	–	–	–
PA 10	E_a	7.9	6.8	7.4	7.9	6.7	5.5
	E_c	–	–	–	–	–	–
	P_{35}^+	43.4	71.6	31.1	12.0	35.0	167.3
	P_{35}^-	–	–	–	–	–	–
	P_{35}^+/P_{35}^-	–	–	–	–	–	–
PA 12	E_a	7.6	8.9	7.1	8.7	6.4	5.7
	E_c	7.4	8.3	11.0	5.7	6.5	4.5
	P_{35}^+	6.4	125.9	52.0	22.5	49.0	304.9
	P_{35}^-	30.3	53.0	42.0	2.6	8.0	35.7
	P_{35}^+/P_{35}^-	2.1	2.4	1.2	8.6	6.1	8.5
PA 14	E_a	5.8	5.7	5.7	6.5	6.5	3.7
	E_c	6.1	6.4	8.7	10.1	8.6	6.6
	P_{35}^+	52.5	96.2	56.5	22.4	65.7	303.1
	P_{35}^-	12.2	14.9	6.6	2.2	4.5	21.3
	P_{35}^+/P_{35}^-	4.3	6.5	8.5	10.3	14.8	14.3
PA 18	E_a	5.4	6.3	5.2	6.3	5.6	2.7
	E_c	6.6	7.1	10.6	12.9	13.1	9.2
	P_{35}^+	68.9	113.4	75.0	29.1	90.9	428.2
	P_{35}^-	8.1	8.2	1.2	0.3	0.6	4.3
	P_{35}^+/P_{35}^-	8.5	13.8	62.7	95.8	143.9	100.1
PA 22	E_a	4.2	2.0	4.0	4.0	4.0	1.5
	E_c	6.8	7.4	9.7	11.6	11.5	8.5
	P_{35}^+	107.2	256.7	92.1	34.9	65.0	461.2
	P_{35}^-	8.7	9.0	1.0	0.3	0.5	4.2
	P_{35}^+/P_{35}^-	12.4	28.5	92.1	120.7	123.0	110.3

Note that the activation energies E_a and E_c have units of kcal/mol while the permeability coefficients P_{35}^+ and P_{35}^- have units of Barrers, i.e.: 10^{-10} $cm^3(STP) - cm/(cm^2 - cmHg - s)$.

approximate density of 0.88 g/cm^3 for amorphous poly(*n*-alkyl acrylates) to obtain the following relationship between d_a (in Å) and n

$$d_a = \sqrt{\frac{(72 + 14n)}{0.51}} \tag{8}$$

The calculated *d*-spacings from the model are shown as the solid line in Fig. 10. The model line has essentially the same slope as the open points but lies slightly below the experimental observations. The latter disparity may be attributed to the assumption that the backbone carbon–carbon bonds are in an all trans conformation whereas many of these bonds will be in gauche positions. The kinks and coils in the main chains resulting from a mixture of trans and gauche conformations cause the average axial length per repeat unit to be less than 2.5 Å, and as a result the measured *d*-spacing should be slightly greater than predicted by the model.

4.2. Copolymers

The characteristic dimensions of the crystalline and amorphous phases of copolymers of various *n*-alkyl acrylate monomers as measured by SAXS are shown in Fig. 12. The *d*-spacing values are plotted in terms of mole fraction of the A22 comonomer for comparisons with the results in Fig. 4. Plotting the data versus weight fraction does not change the overall trends. As the concentration of A22 in the copolymer increases, so does the *d*-spacing of the copolymers indicating a larger crystallite as expected for a longer average side-chain length. The crystalline phase *d*-spacings observed for copolymers shown in Fig. 12(a) reveal similar trends as seen in Fig. 4(b) for the heat of fusion for these copolymers. The greater the difference in the number of carbons in the side chains of the two monomers in a copolymer, the greater the depression in crystal size and in heat of fusion. A plot of ΔH_f versus *d*-spacing for the crystalline copolymers, see Fig. 11(b), shows a similar correlation between crystal size and ΔH_f as observed for homopolymers, see Fig. 11(a).

The amorphous copolymer *d*-spacings, see Fig. 12(b), increase more or less linearly with mole fraction of A22. This is a logical progression for amorphous copolymers that is in accord with the model derived earlier, i.e. the *d*-spacing values should increase with the average side-chain length of the copolymer.

5. Permeation behavior

5.1. Homopolymers

The permeability of small molecules, like gases, in poly(*n*-alkyl acrylates) exhibit a large 'jump' or 'switch effect' over the range of the side-chain crystalline melting [4,5,8,10,16,17]. Fig. 13 illustrates the typical permeation jump for O_2 and CO_2 for the PA 22 homopolymer; for convenient reference, the DSC thermogram is superimposed on this plot. The permeability of these semi-crystalline polymers have been analyzed in terms of a modified two-phase model proposed by Michaels and Bixler [40]. The model suggests that the permeability of a penetrant in a semi-crystalline polymer, P_c, is related to that of the completely amorphous polymer, P_a, by

$$P_c = \frac{P_a(1-\phi)}{\tau\beta} \tag{9}$$

where ϕ is the volume fraction of the crystal phase, τ is a tortuosity factor and β accounts for immobilization of amorphous chain segments by the presence of the crystals. It is assumed that the crystallites are impermeable to the penetrants and, therefore, all gas transport occurs through the molten polymer. Thus, the crystals create a tortuous path for diffusion. The permeability 'jump' occurs as the crystallites melt at the polymer's T_m causing a significant increase in gas transport through the membrane. This correlation between the melting endotherm and the permeation jump is clearly shown in Fig. 13 where the onset and end of the melting peak marks

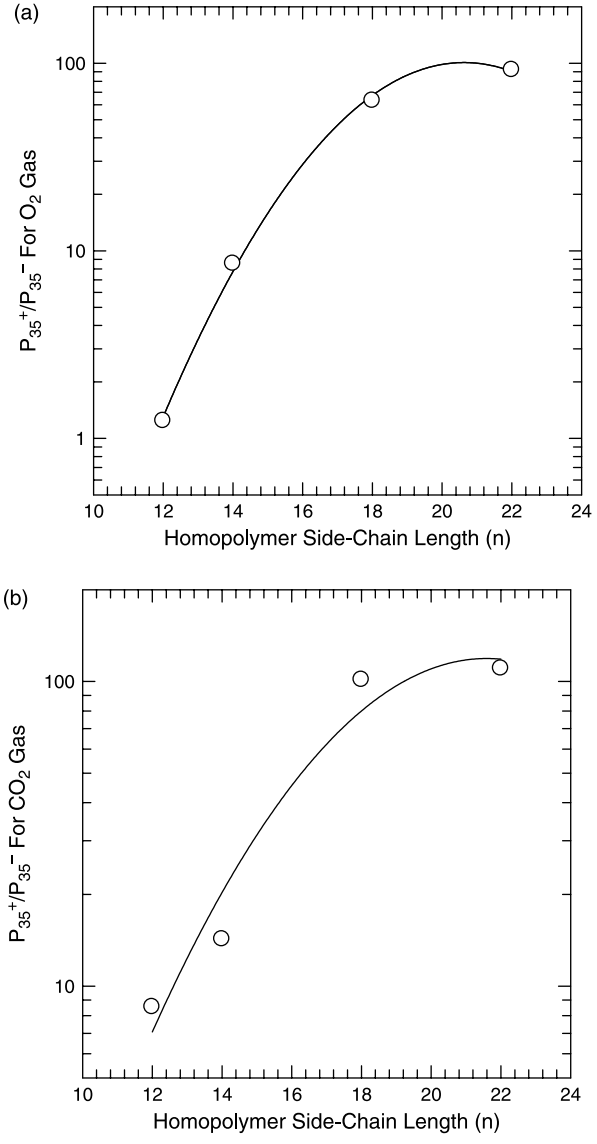

Fig. 15. Homopolymer permeation jump ratios calculated at 35 °C for O_2 (a) and CO_2 (b) gases as a function of side-chain length.

the beginning and end of the permeation jump. Above and below the T_m, permeability increases with temperature in an Arrhenius fashion. At the onset of melting, the permeability jumps nearly two orders of magnitude and returns to an Arrhenious temperature relationship at the end of the melting. The activation energies above and below T_m are different since apparently β (Eq. (9)) depends on temperature. This phenomenon, as reported previously, is reversible and reproducible given the same thermal history [4,5,16]. Although the permeability for six penetrant gases were measured, only O_2 and CO_2 are shown here as examples because they are the most important for modified atmosphere packaging applications.

Similar permeation experiments were conducted on *n*-alkyl acrylate homopolymers with side-chain lengths from 6 to 22 with the results shown in Fig. 14. Various parameters were extracted for comparison and analysis of the permeability data listed in Table 3. The quantities E_a and E_c are the activation energies for permeation in the amorphous and semi-crystalline states, respectively, while P_{35}^{+} and P_{35}^{-} correspond to the molten and crystalline polymers, respectively, extrapolated to 35 °C. Extrapolation to 35 °C is an arbitrary temperature for calculating the jump ratio (P_{35}^{+}/P_{35}^{-}) [16]; however, as explained by Mogri and Paul, the temperature used greatly affects the magnitude of the jump ratios, or calculated jump heights, since the activity energies of the molten and crystalline polymers are not the same. We selected 35 °C because it is near the median melting temperature for the homopolymers and most of the copolymer systems examined later. As the side-chain lengths of the polymers increase, E_a decreases while the permeability and jump ratios increase. These trends were described in detail by Mogri and Paul for similar *n*-alkyl acrylate homopolymers [5,16].

As may be seen in Fig. 14, as the side-chain lengths decrease for these homopolymers, the widths of the permeation jumps increase and gradually flatten out into the simple Arrhenius curves observed for the completely amorphous PA 6 and PA 10. These trends are similar to the endotherm trends for these polymers. As previously discussed, *n*-alkyl acrylate homopolymers with longer side chains are more crystalline than those with shorter side chains. This fact is responsible for the increase in permeation jump ratio with increasing *n* illustrated in Fig. 15. A polymer with a long side-chain has a greater change in morphology at T_m than one with a shorter side chain and, therefore, the permeability jump is greater. It should be emphasized that a significant part of the jump arises because gas molecules must follow a tortuous path around the crystallites; this tortuosity disappears upon melting. The length of this pathway is affected by the lateral dimensions of the crystallites as well as their amount, i.e. crystallinity. At this point there is no simple way to quantify the dimensions, or aspect ratio, of the crystallites, the number of crystallites, or

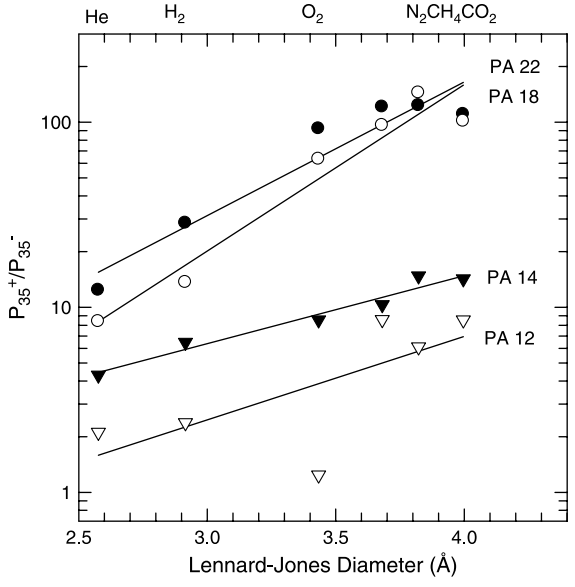

Fig. 16. Permeation jump ratios for various gases calculated at 35 °C for homopolymers with various side-chain lengths as a function of penetrant size.

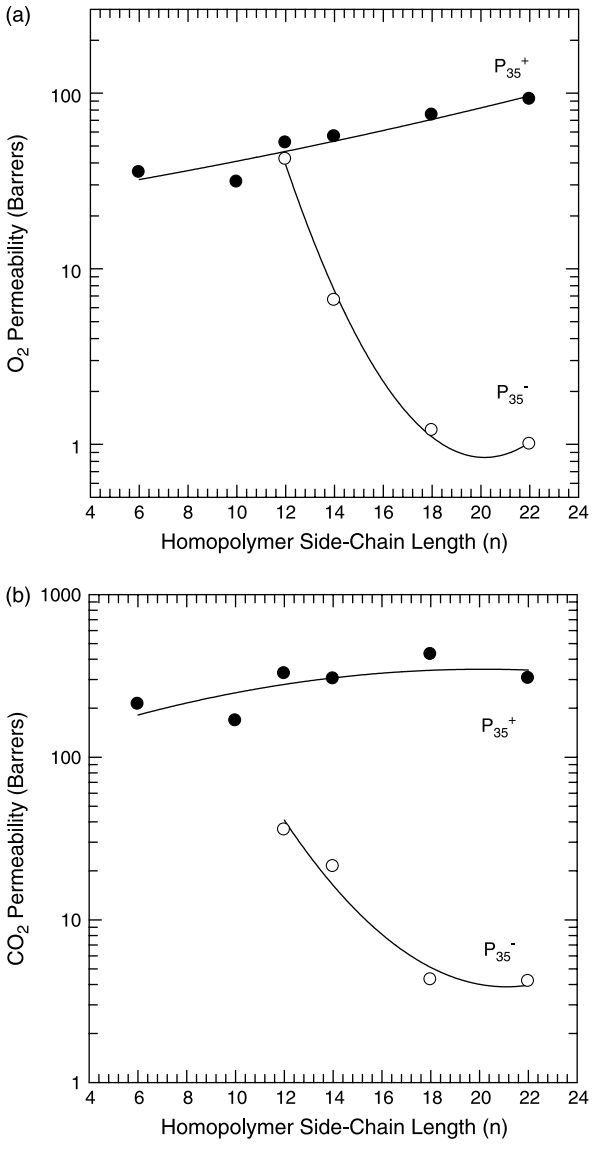

Fig. 17. Permeability of amorphous (P_{35}^{+}) and crystalline (P_{35}^{-}) homopolymers extrapolated to 35 °C for O_2 (a) and CO_2 (b) gas as a function of side-chain length.

their arrangement with respect to one another. While speaking simply of crystallinity clearly does not tell the whole story, it seems that the crystallite dimensions and crystallinity must be closely coupled since the permeability jump seems to be described, at least to a first approximation, by just crystallinity. If the simple geometrical change in the tortuous path on melting were the only factor at play, then, as shown by Mogri and Paul, the permeation jump ratios should be the same for all gases which is not the case [4,5,16]. It seems that the crystallites tend to restrict mobility in the amorphous phase which Michaels and Bixler recognized in main-chain crystalline polymers and modified the conventional two phase model for permeation by including a 'chain immobilization factor', i.e. β, in the equation for permeability in semi-crystalline polymer [40]. In terms of this model, the permeation jump is given by

$$\frac{P_a}{P_c} = \frac{P_{35}^{+}}{P_{35}^{-}} = \frac{\tau\beta}{(1-\phi)} \tag{10}$$

The tortuosity factor should be the same for all penetrants since it is simply a geometric term; however, since the β term reflects changes in segmental dynamics, it may not be the same for all penetrants. Temperature dependence of β would explain why the activation energies for permeation can be larger below T_m than above. The loss of the chain immobilization effect on melting, accounts for much of the permeation jump seen in side-chain crystalline polymers and all of the penetrant size dependence. The increased crystallinity increases the impedance of this conformational freedom in the amorphous backbone. While Fig. 15 only shows data for O_2 and CO_2, Fig. 16 contains data for all the penetrant gases examined in this study. This figure shows the effects of penetrant size on the permeation jump for the various homopolymers. As discussed by Mogri and Paul, the magnitude of the permeation jumps for these semi-crystalline polymers varies greatly with penetrant gas size [4,5,16]. In general, an increase in gas molecular size results in an increase in the jump ratio as shown in Fig. 16. This strong dependence on penetrant size seems to be unique to side-chain crystalline polymers; the jump in permeability on melting main-chain polymers seems to have a much weaker dependence on penetrant size [5,16].

Another informative way to examine the change in permeability on melting is to plot P_{35}^{+} and P_{35}^{-} versus n, see Fig. 17 for O_2 and CO_2 data represented in this way. For both gases, the amorphous permeability increases with n. This increase is due to the increased free volume associated with the additional methylene units of the longer side chains [16]. This

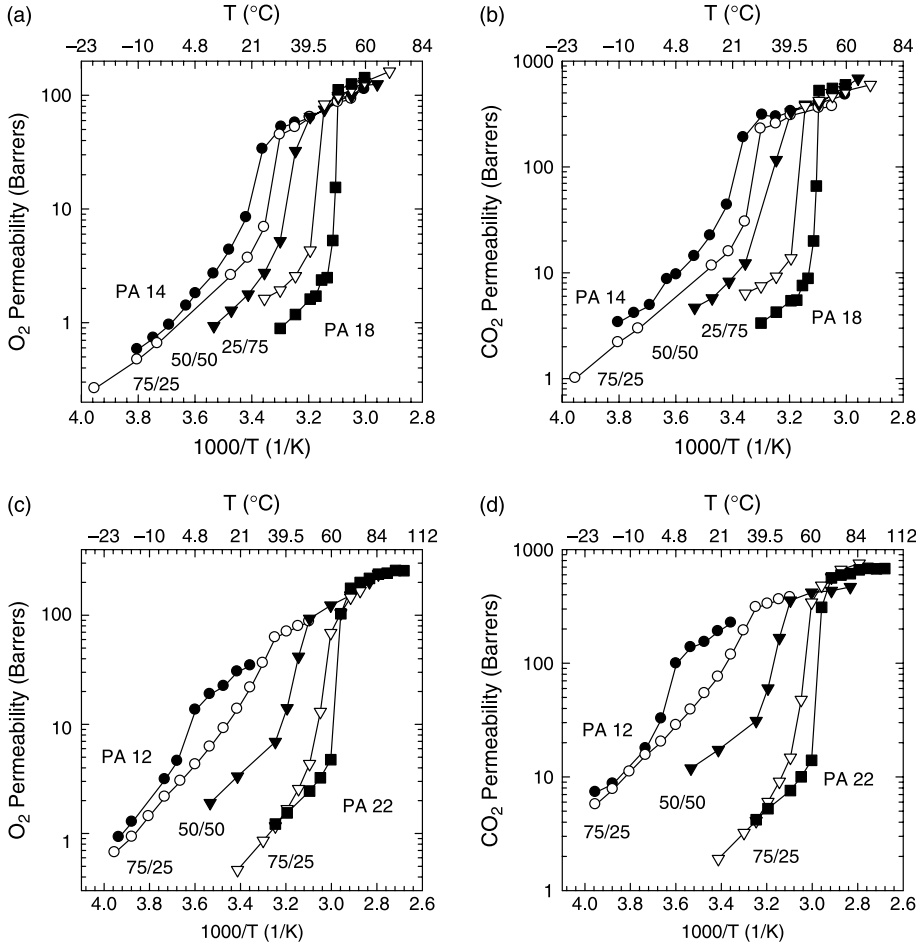

Fig. 18. Permeability of various P(A14-*co*-A18) copolymers to O_2 (a) and CO_2 (b) and P(A12-*co*-A22) copolymers to O_2 (c) and CO_2 (d) as a function of temperature on Arrhenius coordinates.

increase, however, is significantly less than the decrease in permeability of the crystalline polymer with increasing n. The crystalline phase permeability is clearly the dominant contributor to the overall permeation jump ratio for these gases shown in Fig. 15. The crystals act as impenetrable barriers to gas forcing all transport to occur through the amorphous polymer. The increase in side-chain length of the polymers leads to an increase in crystallinity and a decrease in permeability.

5.2. Copolymers

Fig. 18 shows the permeability for O_2 and CO_2 in P(A14-*co*-A18) and P(A12-*co*-A22) copolymers. These plots for copolymers are similar in nature to the plots for homopolymers shown in Fig. 14. For the P(A14-*co*-A18) system, as the average side-chain lengths increases, the magnitude of the permeation jumps increases while the widths of the jumps decreases. Just as the P(A14-*co*-A18) endotherms of Fig. 2(a) resemble the endotherms of *n*-acrylate homopolymers, the permeability trends for this system resemble the homopolymer permeability trends of Fig. 14. The P(A12-*co*-A22) permeation trends follow an analogous pattern; in some cases the behavior is a little more complex than seen for the P(A14-*co*-A18) system. Some of these difference may stem from the larger difference in the length of the side-chain in the comonomers, i.e. $\Delta n = 10$ versus 6. The copolymer containing 75 mol% of A12, in particular, does not show a well-defined Arrhenious relationship in the crystalline phase before the jump begins; for this composition, the permeability jump is rather broad. PA 12 and the copolymer containing 50 mol% A12 do not seem to show such an increase in permeability in the vicinity of T_m.

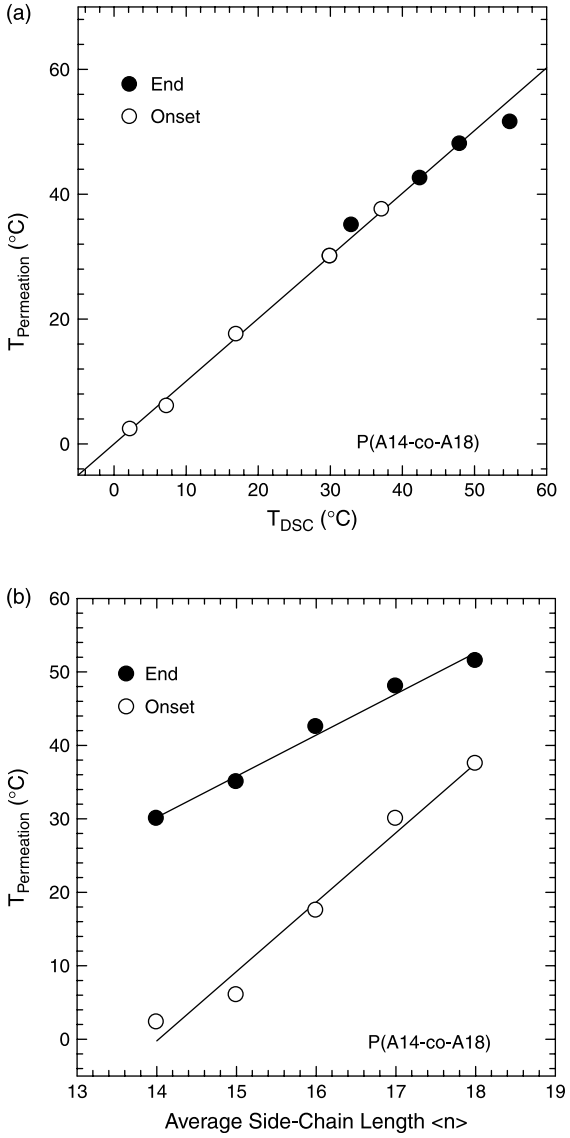

Fig. 19. Relationship between onset and end temperatures for melting of P(A14-*co*-A18) copolymers as measured by permeability jumps and DSC endotherms (a). Correlation between the onset and end temperatures for copolymers of P(A14-*co*-A18) with the average side-chain length (b).

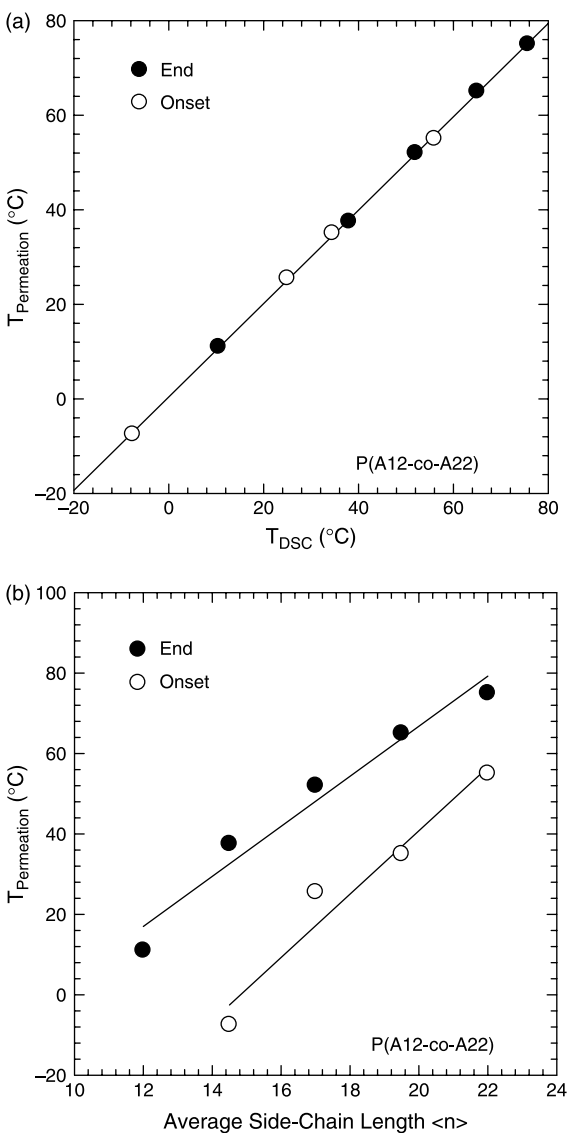

Fig. 20. Relationship between onset and end temperatures for melting of P(A12-*co*-A22) copolymers as measured by permeability jumps and DSC endotherms (a). Correlation between the onset and end temperatures for copolymers of P(A12-*co*-A22) with the average side-chain length (b).

Table 4
Activation energy and permeation data extrapolated to 35 °C for various gases through poly(*n*-alkyl acrylate) copolymers

Copolymer	Mol% monomer 1		Gas					
			He	H_2	O_2	N_2	CH_4	CO_2
P(A10-*co*-A14)	75	E_a	3.5	2.2	4.2	4.9	5.8	3.1
		E_c	–	–	–	–	–	–
		P^+_{35}	57.8	86.7	49.5	17.2	29.5	212.0
		P^-_{35}	–	–	–	–	–	–
		P^+_{35}/P^-_{35}	–	–	–	–	–	–
P(A10-*co*-A14)	50	E_a	6.6	4.4	7.9	8.1	8.6	5.4
		E_c	–	–	–	–	–	–
		P^+_{35}	0.0	68.5	60.9	19.5	50.2	302.2
		P^-_{35}	–	–	–	–	–	–
		P^+_{35}/P^-_{35}	–	–	–	–	–	–
P(A10-*co*-A14)	25	E_a	5.1	3.6	4.8	7.9	8.3	2.7
		E_c	4.4	3.0	6.5	6.5	4.8	5.1
		P^+_{35}	58.1	91.5	66.8	21.7	56.5	308.0
		P^-_{35}	18.2	14.6	11.7	2.3	2.6	44.9
		P^+_{35}/P^-_{35}	3.2	6.2	5.7	9.6	21.6	6.9
P(A10-*co*-A18)	75	E_a	8.3	8.1	6.6	9.4	6.6	4.9
		E_c	–	–	–	–	–	–
		P^+_{35}	46.5	45.7	41.4	48.8	41.5	225.0
		P^-_{35}	–	–	–	–	–	–
		P^+_{35}/P^-_{35}	–	–	–	–	–	–
P(A10-*co*-A18)	50	E_a	7.6	8.2	6.4	9.0	10.4	7.3
		E_c	–	–	–	–	–	–
		P^+_{35}	56.8	98.6	49.6	21.2	58.3	291.1
		P^-_{35}	–	–	–	–	–	–
		P^+_{35}/P^-_{35}	–	–	–	–	–	–
P(A10-*co*-A18)	25	E_a	6.4	6.1	5.4	6.5	6.0	3.4
		E_c	7.3	8.5	9.4	11.5	10.6	7.8
		P^+_{35}	78.1	137.3	55.4	17.7	42.4	272.0
		P^-_{35}	18.7	23.1	4.9	1.6	3.6	21.6
		P^+_{35}/P^-_{35}	4.2	6.0	11.3	11.0	11.7	12.6
P(A14-*co*-A18)	75	E_a	6.3	6.4	5.9	6.2	5.7	3.7
		E_c	7.6	7.4	9.9	13.1	12.7	10.3
		P^+_{35}	67.8	67.1	53.5	22.5	55.7	265.1
		P^-_{35}	12.4	12.0	8.0	3.1	8.1	37.5
		P^+_{35}/P^-_{35}	5.5	5.6	6.7	7.2	6.9	7.1
P(A14-*co*-A18)	50	E_a	6.6	6.0	4.5	5.6	7.2	6.0
		E_c	5.2	7.6	10.5	11.6	11.1	9.3
		P^+_{35}	54.0	194.0	66.8	19.4	51.0	273.4
		P^-_{35}	8.4	13.1	4.3	1.2	2.5	17.5
		P^+_{35}/P^-_{35}	6.4	7.2	15.7	16.7	20.5	15.6
P(A14-*co*-A18)	25	E_a	6.3	6.0	5.5	7.1	4.7	4.0
		E_c	7.3	8.1	4.6	6.9	12.3	4.7
		P^+_{35}	69.6	105.8	65.4	20.9	66.1	311.2
		P^-_{35}	9.1	9.0	2.2	0.6	1.3	8.8
		P^+_{35}/P^-_{35}	7.6	11.7	30.4	34.8	49.4	34.6
P(A12-*co*-A22)	75	E_a	4.3	4.1	4.5	3.8	5.6	2.7
		E_c	7.7	8.6	10.1	9.9	10.3	6.4
		P^+_{35}	118.2	204.0	62.3	22.4	43.6	267.2
		P^-_{35}	48.3	76.5	23.3	5.3	20.1	50.1
		P^+_{35}/P^-_{35}	2.5	2.7	2.7	4.2	2.2	5.2
P(A12-*co*-A22)	50	E_a	3.1	3.3	5.8	4.7	6.0	1.3
		E_c	7.8	8.3	8.9	9.1	12.3	6.7
		P^+_{35}	127.5	188.7	59.8	21.1	33.2	352.9
		P^-_{35}	31.5	38.4	7.0	2.1	5.0	30.9
		P^+_{35}/P^-_{35}	4.0	4.9	8.6	9.9	6.6	11.4
P(A12-*co*-A22)	25	E_a	6.2	8.1	4.0	4.0	4.0	1.5
		E_c	7.8	8.1	11.0	9.2	12.3	9.2
		P^+_{35}	85.3	89.7	77.1	19.6	37.5	375.4
		P^-_{35}	7.3	7.3	1.2	0.3	0.8	4.1
		P^+_{35}/P^-_{35}	11.7	12.3	66.5	57.2	46.8	91.5

Note that monomer 1 refers to the first monomer listed in the copolymer, i.e. for P(A14-*co*-A18), monomer 1 refers to A14. All units are the same as in Table 3.

The endotherms for this system were similar to those of P(A10-*co*-A18) in Fig. 2(b) where the distribution of crystallite sizes in the copolymer broadens with increasing concentration of the shorter monomer. This broadening and reduction of the height of the melting peak appears to be the cause for the gradual increase in permeability as the T_m is approached in the case of the 75 mol% A12 copolymer.

It turns out that DSC thermograms are a simple and effective way to predict the breadth of the permeation jump as the copolymer melting point is traversed, as shown in Figs. 19 and 20 for P(A14-*co*-A18) and P(A12-*co*-A22) copolymers. Figs. 19(a) and 20(a) compare the onset and end temperature of the melting peak, as measured using DSC, to the onset and end temperatures of the permeability jump. The baseline construction method used to define the DSC onset and end points was described in a previous publication [8]. The onset and end of the permeability jump was defined by drawing the Arrhenious relationship for the pre- and post-melt permeabilities and locating the temperature where the permeability deviates from the Arrhenius line. As seen in Figs. 19(a) and 20(a), there is an excellent linear relationship between the temperatures obtained by DSC and by permeation experiments. This is a significant relationship in that simple DSC experiments can be used to judge the breadth of the permeability jump since changes in copolymer crystallinity define the permeation response. The onset and end temperatures measured by permeability are plotted as a function of average side chain length in Figs. 19(b) and 20(b). The difference between the onset and end temperatures for both copolymer systems tend to narrow as the side-chain length increases. This is consistent with the thermal and structural analysis of these systems; as the side-chain length increases, the melting peak becomes more narrow which suggests a more narrow size distribution of crystallites.

Table 4 summarizes the activation energies for the molten and crystalline copolymers, their absolute permeability to six gases and the permeability jump ratios evaluated at 35 °C. Fig. 21 shows how the jump ratio for P(A14-*co*-A18) and P(A12-*co*-A22) copolymers depend on copolymer composition and penetrant size. As in Fig. 16 for homopolymers, the copolymer systems show larger permeation jumps with larger penetrant diameter and longer average side-chain length. Surprisingly, however, for both systems, the homopolymer with the shorter side chains tend to show a larger permeability jump ratio than the does the copolymer containing 25 mol% of the monomer with the longer side-chain for gases with diameters larger than hydrogen. Fig. 22 shows the jump ratios at 35 °C for O_2 and CO_2 as a function of the average side-chain length for P(A12-*co*-A22) copolymers. The points represent the copolymer data while the line represents the homopolymer data from Fig. 15. In all cases shown, the copolymers exhibit somewhat smaller permeation jumps than do the homopolymers. The P(A14-*co*-A18) copolymer system shows smaller differences between the homopolymers and copolymers than does the P(A12-*co*-A22) system [41], as might be expected based on differences in the side-chain lengths for the two systems. The ΔH_f from thermal analysis and *d*-spacings from the SAXS analysis reveal a progressively lower value for the

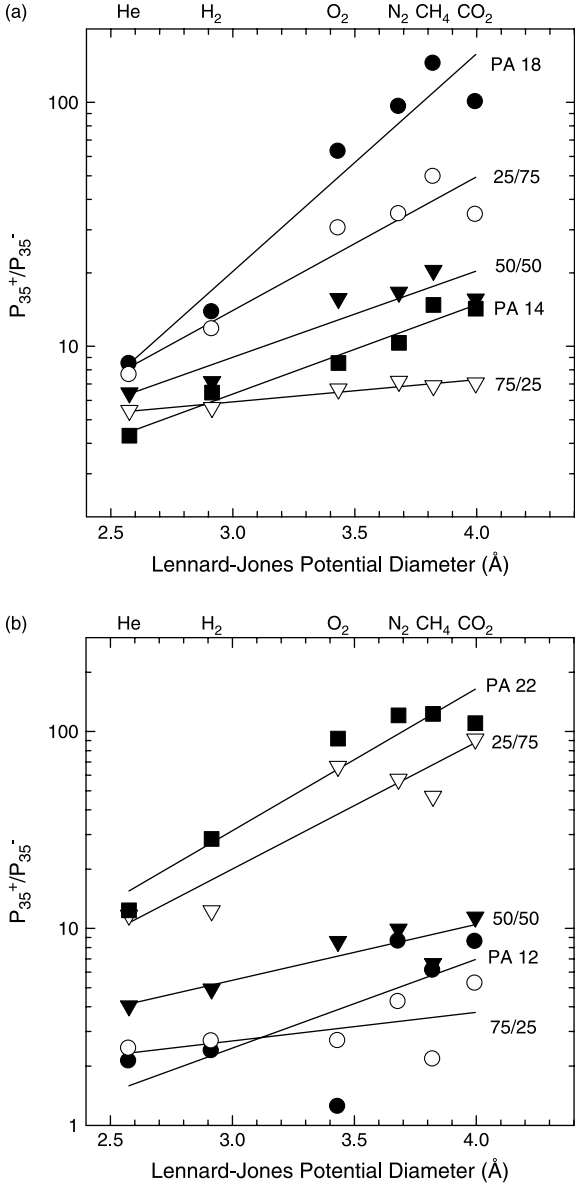

Fig. 21. Permeation jump ratios calculated at 35 °C for P(A14-*co*-A18) (a) and P(A12-*co*-A22) (b) copolymers as a function of side-chain length of the penetrant molecule.

copolymer than the homopolymer at the same values of *n* with homopolymer-copolymer differences increasing as the differences in length of the side chains in the two copolymers becomes larger. This trend translates to the permeability jump ratio. Thus, even though there is evidence that the copolymers co-crystallize, it appears that there is some loss in crystallinity, and perhaps crystallite aspect ratio, compared to homopolymers of the same *n* and the effect grows as Δn becomes larger.

Fig. 23 compares P_{35}^{+} and P_{35}^{-} for O_2 and CO_2 for P(A14-*co*-A18) copolymers to that of homopolymers. This type of plot is useful since it shows that the permeability jump ratio is primarily a result of the reduction in the permeability below the melting point as n increases, and to a lesser extent, the increase in permeability in the molten state as n increases. In addition, these plots provide a means of comparing the crystalline effects

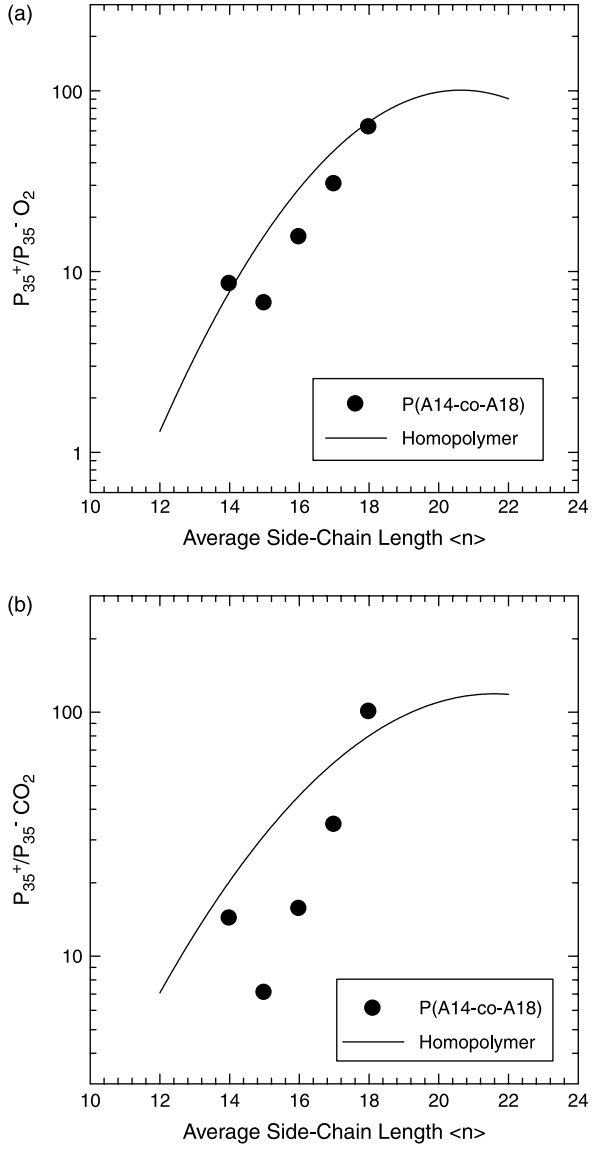

Fig. 22. Comparison of permeation jump ratios for homopolymers (lines) with P(A14-*co*-A18) copolymers (points) calculated at 35 °C for O_2 (a) and CO_2 (b) gases.

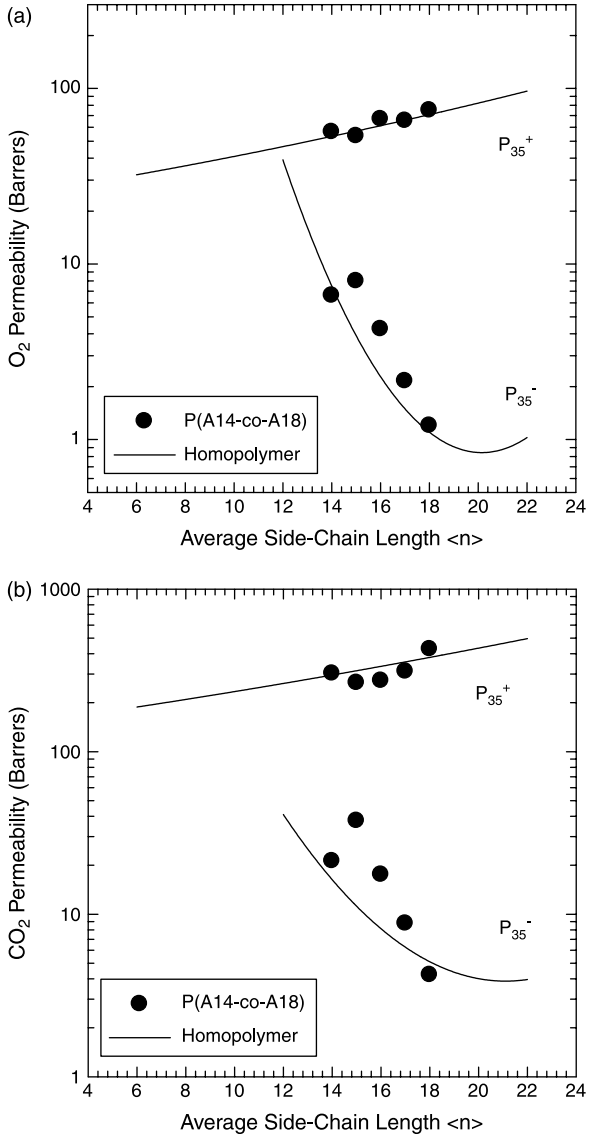

Fig. 23. Comparison of the O_2 (a) and CO_2 (b) permeability of amorphous (P_{35}^+) and crystalline (P_{35}^-) homopolymers (lines) and P(A14-*co*-A18) copolymers (points) calculated at 35 °C as a function of side-chain length.

on permeability jump for homopolymers and copolymers. In Fig. 23, the permeability through molten P(A14-*co*-A18) copolymers, shown as solid circles, clearly align with the molten homopolymer data, taken from Fig. 17, shown as the lines. This is also true for the permeability of molten P(A12-*co*-A22) copolymers [41]. The permeability of crystalline P(A14-*co*-A18) copolymers deviates slightly from the homopolymer data; the maximum deviation occurs at 75 mol% A14 copolymer. At this composition, there is an increased permeability through the crystalline polymer compared to PA 14. This increased permeability, caused by a decrease in crystallinity, is reflected in the diminished jump ratio of Figs. 21(a) and 22. P(A12-*co*-A22) copolymers show an even greater deviation from the crystalline homopolymer data [41]. This is due to the decrease in crystallinity of this copolymer system, as seen from the ΔH_f and *d*-spacing results in Figs. 4(b) and 12(a). This increase in crystalline permeability is the compelling factor in the decreased jump ratio for this system shown in Fig. 21(b).

6. Conclusions

Poly(*n*-alkyl acrylate) homopolymer and copolymer systems comprised of two crystallizeable monomer units were studied with respect to their thermal behavior, structural composition, and gas permeability properties. The thermal properties of the homopolymers show a direct correlation between the T_m and ΔH_f and side-chain length. The copolymers exhibit isomorphic behavior with similar relationships between T_m and ΔH_f and the average side-chain length as seen for the homopolymers. The copolymers, however, did exhibit some depression in ΔH_f relative to that of the homopolymers, which increases as the difference in the number of carbons in the side chains of the two monomers

increases. This qualitatively measures the reduction in crystallite size for the copolymers as a function of composition. Small angle X-ray scattering measurements were made on homopolymer and copolymer systems of varying side-chain length. The *d*-spacing values of the crystalline homopolymers were measured and described by a simple model. A simple molecule packing model was proposed that will reasonably predict the amorphous *d*-spacing as a function of side-chain length. Crystalline copolymers showed nearly identical trends of *d*-spacing with composition as seen for the heat of fusion. Amorphous copolymers show a nearly linear relationship between *d*-spacing and composition as expected from the simple packing model. Permeability measurements for the homopolymers and copolymers exhibit the signature 'jump' in permeability as the T_m is transversed. Comparison between DSC thermograms and gas permeability of the polymers over a range of temperatures revealed a correlation between both the width of the permeability jumps and endotherms as well as the permeation jump ratio and crystallinity. Ultimately, DSC endotherms are an excellent tool for predicting the permeation jump behavior of *n*-alkyl acrylate homopolymers and copolymers comprised of two crystallizeable monomers. The heat of fusion provides qualitative insight about the magnitude of the permeability jump.

Acknowledgements

This research was funded by National Science Foundation Grant number CTS-0086961 administered by the Division of Chemical and Transport Systems-Separation and Purification Processes Program.

References

[1] Rehberg CE, Fisher CH. J Am Chem Soc 1944;66:1203.
[2] Hirabayashi T, Kikuta T, Kasabou K, Yokota K. Polym J 1988;20(8):693.
[3] Plate NA, Shibaev VP. Comb-shaped polymers and liquid crystals. New York: Plenum Press; 1987 p. 1–104.
[4] Mogri Z, Paul DR. Polymer 2000;42(6):2531–42.
[5] Mogri Z. PhD Thesis, University of Texas at Austin; 2001.
[6] Jordan Jr EF, Feldeisen DW, Wrigley AN. J Polym Sci, Polym: Chem Ed 1971;9(7):1835.
[7] Clark R, Stewart R, Yoon V, Schultz D, McClary B. US Patent No. 96-US7939, Landec Corporation, USA; 1996.
[8] O'Leary K, Paul DR. Polymer 2004;45(19):6575.
[9] Mogri Z, Paul DR. J Membr Sci 2000;175(2):253.
[10] Clark R, Stewart R, Yoon V, Schultz D, McClary B. US Patent No. 453018, Landec Corporation, USA; 2002.
[11] Stewart RF. US Patent No. 87-120399, Landec Labs., Inc., USA; 1989.
[12] Greenberg SA, Alfrey T. J Am Chem Soc 1954;76:6280.
[13] Hirabayash T, Yokota K. Polym J 1987;19(9):1115.
[14] Greene L, Phan L, Schmitt E, Mohr J. ACS Symp Ser 1993;520:244.
[15] Kirkland BS, Paul DR. Unpublished results.
[16] Mogri Z, Paul DR. Polymer 2001;42(18):7765.
[17] Paul DR, Clarke R. J Membr Sci 2002;208(1–2):269.
[18] Bitler SP, Stewart R, Kamp D, Meyers P, Taft D, Schultz D. US Patent No. 97-US16019, Landec Corp., USA; 1998.
[19] Meyers PA, Dorman LC. US Patent No. 86-871002, Dow Chemical Co., USA; 1989.
[20] Lioutus TS. Food Tech 1988;78.
[21] Zagory D. Food Tech 1988;70.
[22] Church IJ, Parsons AL. J Sci Food Agric 1995;67(2):143.
[23] Young GL. Ann Tech Conf Soc Plastic Eng 1995;53(vol. 2):2234.
[24] Exama A, Arul J, Lencki RW, Lee LZ, Toupin C. J Food Sci 1993;58(6):1365.
[25] Sanchez IC, Eby RK. J Res Natl Bur Stand Sec A: Phys Chem 1973;77(3):353.
[26] Kamiya N, Sakurai M, Inoue Y, Chujo R. Macromolecules 1991;24(13):3888.
[27] Edgar OB, Hill R. J Polym Sci 1952;8:1.
[28] Harris JE, Robeson LM. J Polym Sci, Part B 1987;25(2):311.
[29] Kim MS, Levon K. J Polym Sci, Part B 1996;34(9):1665.
[30] Pal S, Nandi AK. Macromolecules 2003;36(22):8426.
[31] Kim MS, Levon K. J Polym Sci, Part B 1997;35(7):1025.
[32] Miyazaki T, Kaneko T, Gong J, Osada Y. Macromolecules 2001;34(17):6024.
[33] Shi H, Zhao Y, Zhang X, Zhou Y, Xu Y, Zhou S, et al. Polymer 2004;45(18):6299.
[34] Luyten MC, Alberta van Ekenstein G, Ten Brinke G, Roukolainen J, Ikkala O, Torkkeli M, et al. Macromolecules 1999;32(13):4404.
[35] Hsieh HWS, Post B, Morawetz H. J Polym Sci, Polym Phys 1976;14(7):1241.
[36] Hsieh HWS. PhD Thesis. Polytechnic Inst. of New York; 1976.
[37] Fairclough JPA, Hamley IW, Terrill NJ. Radiat Phys Chem 1999;56(1–2):159.
[38] Hadjichristidis N, Pispas S, Floudas G. Block copolymers. 1st ed. Hoboken: Wiley; 2003 p. 347.
[39] Chu B, Hsiao BS. Chem Rev 2001;101(6):1727.
[40] Michaels AS, Bixler HJ. J Polym Sci 1961;50:413.
[41] O'Leary KA. PhD Dissertation. The University of Texas at Austin; 2005.